

REPORT DOCUMENTATION PAGE			Form Approved OMB NO. 0704-0188		
<p>The public reporting burden for this collection of information is estimated to average 1 hour per response, including the time for reviewing instructions, searching existing data sources, gathering and maintaining the data needed, and completing and reviewing the collection of information. Send comments regarding this burden estimate or any other aspect of this collection of information, including suggestions for reducing this burden, to Washington Headquarters Services, Directorate for Information Operations and Reports, 1215 Jefferson Davis Highway, Suite 1204, Arlington VA, 22202-4302. Respondents should be aware that notwithstanding any other provision of law, no person shall be subject to any penalty for failing to comply with a collection of information if it does not display a currently valid OMB control number.</p> <p>PLEASE DO NOT RETURN YOUR FORM TO THE ABOVE ADDRESS.</p>					
1. REPORT DATE (DD-MM-YYYY) 29-07-2015		2. REPORT TYPE Final Report		3. DATES COVERED (From - To) 1-Aug-2014 - 30-Apr-2015	
4. TITLE AND SUBTITLE Final Report: Network-Theoretic Modeling of Fluid Flow			5a. CONTRACT NUMBER W911NF-14-1-0386		
			5b. GRANT NUMBER		
			5c. PROGRAM ELEMENT NUMBER 611102		
6. AUTHORS Kunihiko Taira			5d. PROJECT NUMBER		
			5e. TASK NUMBER		
			5f. WORK UNIT NUMBER		
7. PERFORMING ORGANIZATION NAMES AND ADDRESSES Florida State University Sponsored Research Administration 874 Traditions Way, Third Floor Tallahassee, FL 32306 -4166			8. PERFORMING ORGANIZATION REPORT NUMBER		
9. SPONSORING/MONITORING AGENCY NAME(S) AND ADDRESS (ES) U.S. Army Research Office P.O. Box 12211 Research Triangle Park, NC 27709-2211			10. SPONSOR/MONITOR'S ACRONYM(S) ARO		
			11. SPONSOR/MONITOR'S REPORT NUMBER(S) 65650-NS-II.2		
12. DISTRIBUTION AVAILABILITY STATEMENT Approved for Public Release; Distribution Unlimited					
13. SUPPLEMENTARY NOTES The views, opinions and/or findings contained in this report are those of the author(s) and should not be construed as an official Department of the Army position, policy or decision, unless so designated by other documentation.					
14. ABSTRACT A network-theoretic framework has been developed to model unsteady flows. Network analysis has been utilized to examine a wide variety of large-scale problems, including control of disease transmission, robust operation of power grids/internet, and uncovering brain functionality. The present investigation extends the network-theoretic approaches to describe the complex nonlinear behavior of unsteady fluid flows with particular focus on vortex interaction and modal energy transfer. Three canonical unsteady fluid flow problems are examined with network analysis: (1) discrete vortex dynamics, (2) modal interaction during wake formation in cylinder flow, and (3) two					
15. SUBJECT TERMS Network analysis, unsteady fluid flows, vortex dynamics, turbulence					
16. SECURITY CLASSIFICATION OF:			17. LIMITATION OF ABSTRACT UU	15. NUMBER OF PAGES	19a. NAME OF RESPONSIBLE PERSON Kunihiko Taira
a. REPORT UU	b. ABSTRACT UU	c. THIS PAGE UU			19b. TELEPHONE NUMBER 850-645-0140



## Report Title

Final Report: Network-Theoretic Modeling of Fluid Flow

### ABSTRACT

A network-theoretic framework has been developed to model unsteady flows. Network analysis has been utilized to examine a wide variety of large-scale problems, including control of disease transmission, robust operation of power grids/internet, and uncovering brain functionality. The present investigation extends the network-theoretic approaches to describe the complex nonlinear behavior of unsteady fluid flows with particular focus on vortex interaction and modal energy transfer. Three canonical unsteady fluid flow problems are examined with network analysis: (1) discrete vortex dynamics, (2) modal interaction during wake formation in cylinder flow, and (3) two-dimensional isotropic homogeneous turbulence. Graph theory is utilized to extract important fluid flow interactions, which enabled the development of a sparsified vortex dynamics model. The network-based approach to examine the energy transfer between modal fluid flow structures has allowed for intuitive understanding of how perturbation or control input can alter the dynamics of the global fluid flow. At last, it was revealed that two-dimensional turbulence has an underlying scale-free network structure. The findings from the present study lay out a foundation to perform further network-based characterization and control to modify the collective behavior of unsteady fluid flows.

---

**Enter List of papers submitted or published that acknowledge ARO support from the start of the project to the date of this printing. List the papers, including journal references, in the following categories:**

#### **(a) Papers published in peer-reviewed journals (N/A for none)**

Received

Paper

07/29/2015	1.00	Aditya G. Nair, Kunihiro Taira. Network-theoretic approach to sparsified discrete vortex dynamics, Journal of Fluid Mechanics, (03 2015): 549. doi: 10.1017/jfm.2015.97
------------	------	---

**TOTAL:        1**

**Number of Papers published in peer-reviewed journals:**

---

#### **(b) Papers published in non-peer-reviewed journals (N/A for none)**

Received

Paper

**TOTAL:**

**Number of Papers published in non peer-reviewed journals:**

---

#### **(c) Presentations**

1. A. Nair and K. Taira, "Network-theoretic approach to model vortex interactions" APS-DFD, San Francisco, Nov, 2014.
2. K. Taira and A. Nair, "Sparsified-dynamics modeling of discrete point vortices with graph theory", APS-DFD, San Francisco, Nov. 2014.

Number of Presentations: 2.00

---

**Non Peer-Reviewed Conference Proceeding publications (other than abstracts):**

Received      Paper

**TOTAL:**

Number of Non Peer-Reviewed Conference Proceeding publications (other than abstracts):

---

**Peer-Reviewed Conference Proceeding publications (other than abstracts):**

Received      Paper

**TOTAL:**

Number of Peer-Reviewed Conference Proceeding publications (other than abstracts):

---

**(d) Manuscripts**

Received      Paper

**TOTAL:**



Number of Manuscripts:

Books

Received      Book

TOTAL:

Received      Book Chapter

TOTAL:

Patents Submitted

Patents Awarded

Awards

Graduate Students

<u>NAME</u>	<u>PERCENT SUPPORTED</u>	Discipline
Aditya Nair	1.00	
<b>FTE Equivalent:</b>	<b>1.00</b>	
<b>Total Number:</b>	<b>1</b>	

Names of Post Doctorates

<u>NAME</u>	<u>PERCENT SUPPORTED</u>
Alejandro Rivera Alvarez	0.63
<b>FTE Equivalent:</b>	<b>0.63</b>
<b>Total Number:</b>	<b>1</b>

---

### Names of Faculty Supported

<u>NAME</u>	<u>PERCENT SUPPORTED</u>	National Academy Member
Kunihiko Taira	0.01	
<b>FTE Equivalent:</b>	<b>0.01</b>	
<b>Total Number:</b>	<b>1</b>	

### Names of Under Graduate students supported

<u>NAME</u>	<u>PERCENT SUPPORTED</u>
<b>FTE Equivalent:</b>	
<b>Total Number:</b>	

### Student Metrics

This section only applies to graduating undergraduates supported by this agreement in this reporting period

The number of undergraduates funded by this agreement who graduated during this period: ..... 0.00

The number of undergraduates funded by this agreement who graduated during this period with a degree in science, mathematics, engineering, or technology fields:..... 0.00

The number of undergraduates funded by your agreement who graduated during this period and will continue to pursue a graduate or Ph.D. degree in science, mathematics, engineering, or technology fields:..... 0.00

Number of graduating undergraduates who achieved a 3.5 GPA to 4.0 (4.0 max scale):..... 0.00

Number of graduating undergraduates funded by a DoD funded Center of Excellence grant for Education, Research and Engineering:..... 0.00

The number of undergraduates funded by your agreement who graduated during this period and intend to work for the Department of Defense ..... 0.00

The number of undergraduates funded by your agreement who graduated during this period and will receive scholarships or fellowships for further studies in science, mathematics, engineering or technology fields: ..... 0.00

---

### Names of Personnel receiving masters degrees

<u>NAME</u>
<b>Total Number:</b>

### Names of personnel receiving PHDs

<u>NAME</u>
<b>Total Number:</b>

### Names of other research staff

<u>NAME</u>	<u>PERCENT SUPPORTED</u>
<b>FTE Equivalent:</b>	
<b>Total Number:</b>	

---

Sub Contractors (DD882)

**Inventions (DD882)**

**Scientific Progress**

**Technology Transfer**

**Final Report**  
**STIR: Network-Theoretic Modeling of Fluid Flow**

ARO Grant W911NF-14-1-0386  
Program manager: Dr. Samuel Stanton  
(August 1, 2014–April 30, 2015)

PI: Kunihiro Taira  
*Department of Mechanical Engineering*  
*Florida A&M/Florida State University, Tallahassee, FL 32310*

**Abstract**

A network-theoretic framework has been developed to model unsteady flows. Network analysis has been utilized to examine a wide variety of large-scale problems, including control of disease transmission, robust operation of power grids/internet, and uncovering brain functionality. The present investigation extends the network-theoretic approaches to describe the complex nonlinear behavior of unsteady fluid flows with particular focus on vortex interaction and modal energy transfer. Three canonical unsteady fluid flow problems are examined with network analysis: (1) discrete vortex dynamics, (2) modal interaction during wake formation in cylinder flow, and (3) two-dimensional isotropic homogeneous turbulence. Graph theory is utilized to extract important fluid flow interactions, which enabled the development of a sparsified vortex dynamics model. The network-based approach to examine the energy transfer between modal fluid flow structures has allowed for intuitive understanding of how perturbation or control input can alter the dynamics of the global fluid flow. At last, it was revealed that two-dimensional turbulence has an underlying scale-free network structure. The findings from the present study lay out a foundation to perform further network-based characterization and control to modify the collective behavior of unsteady fluid flows.

## Contents

<b>1</b>	<b>Introduction</b>	<b>3</b>
1.1	Objective and Accomplishments . . . . .	3
1.2	Background . . . . .	3
1.3	Network-Theoretic Framework . . . . .	4
<b>2</b>	<b>Network Representation of Discrete Vortex Interactions</b>	<b>6</b>
2.1	Representing Vortex Interactions on a Graph . . . . .	6
2.2	Spectral Sparsification . . . . .	7
2.3	Sparsification of Vortex Interactions . . . . .	9
2.4	Sparsified-Dynamics Model . . . . .	13
2.5	Conservation Properties . . . . .	19
2.6	Sparsified-Dynamics Model and Reduced-Order Model . . . . .	20
<b>3</b>	<b>Energy Transfer in Modal Network of Fluid Flow</b>	<b>22</b>
3.1	Modal Energy Interaction Analysis . . . . .	22
3.2	Network Representation of Modal Energy Interaction . . . . .	24
3.3	Application to Linear to Nonlinear Transitional Flow . . . . .	24
3.4	Feedback Control of Modal Fluid Flow Network . . . . .	26
<b>4</b>	<b>Two-Dimensional Turbulence Network</b>	<b>28</b>
4.1	Network Analysis Setup . . . . .	29
4.2	Scale-Free Characteristics of Two-Dimensional Turbulence . . . . .	30
<b>5</b>	<b>Summary</b>	<b>31</b>
<b>6</b>	<b>Personnel</b>	<b>31</b>
<b>7</b>	<b>Acknowledgments</b>	<b>31</b>
	<b>References</b>	<b>31</b>

# 1 Introduction

## 1.1 Objective and Accomplishments

The objective of this STIR research was to develop a network-theoretic framework to model unsteady vortex-dominated flows. To achieve the goals of this project, we have considered modeling and analysis of three canonical fluid flow problems; namely (1) discrete vortex dynamics, (2) unsteady laminar flow, and (3) two-dimensional turbulence. Within the 9-month performance period, we have been able to examine a discrete vortex dynamics problem in detail and develop a sparsified dynamics model. Furthermore, we were able to make headways in obtaining preliminary results in capturing energy transfers in unsteady laminar flows and characterizing turbulent flow using network analysis.

In particular, we have been able to accomplish the following items:

### 1. Network representation of discrete vortex interactions

Established network representations of discrete vortex dynamics in two-dimensional flow. Identified key vortex-to-vortex interactions through use of graph-theoretic techniques. Constructed a *sparsified-dynamics model* based on spectral graph theory to create computationally inexpensive representation of full nonlinear dynamics.

### 2. Examination of energy transfer in modal network of fluid flow

Performed reduced-order modeling of two-dimensional flow over a cylinder using proper orthogonal decomposition mode based Galerkin projection. Modal network representations are constructed to track the energy flow between the modes. Feedback control was employed to force the flow to the base state and their implications on network interactions of the modes were examined.

### 3. Characterization of two-dimensional turbulence

Analyzed the network structure of two-dimensional isotropic homogeneous turbulence. It was found that turbulent flow was an underlying scale-free network that characterizes the vortical interactions.

## 1.2 Background

Network describes how components are linked to one another. We can represent the components by points (nodes) and the connections by lines (edges) through a mathematical abstraction. The structure comprised of these nodes and edges is called a graph, which has been studied in detail in the field of graph theory [1]. Network analysis is concerned with the study of graphs as well as the interaction and evolution of the variables of interest on graphs over time and space [2]. The framework developed in network analysis and graph theory can provide insights into how the structure of a network can influence the overall dynamics taking place on the network.

Network analysis and graph theory by nature are very fundamental and generic, which enable them to impact a wide range of applications, including the analysis of biological and social networks, study of traffic flows, and design of robust power grids [2]. Biologists and medical scientists use network analysis to determine how electrical signals travel inside the brain and how abnormality in the brain network connections can affect the normal functionality [3, 4]. In epidemiology, researchers model the outbreak of diseases on the population network. Locations with high concentration of population, such as airports, stations, schools, and hospitals, can be represented on a network with large number of connections. Identifying such locations is especially critical when containment

measures are designed to control outbreaks of HIV [5], SARS [6], and Influenza [7, 8]. Each of these diseases has different dynamics and an associated network structure. Once the high-risk groups and areas are identified, network analysis can assist in designing and implementing prevention and combat strategies in the swiftest manner with limited resources [9, 10]. Network analysis can also reveal how a group of people are socially connected to one another and examine how subgroups within a population are interlinked in a complex manner [11]. Moreover, network analysis has been utilized in electrical engineering to determine the voltages and currents associated with electrical circuits via graph representations [12]. In the aforementioned applications of network analysis, the connections between people or elements are highlighted.

The dynamics of unsteady fluid flow is governed by nonlinear interactions. This is especially true for turbulent flows resulting in multi-scale interaction problems. While there has been tremendous advancements made in the areas of numerical simulations and stability analysis in fluid mechanics [13, 14, 15], there has been limited work highlighting the nonlinear interactions responsible for the collective dynamics of fluid structures or vortices. In the present work, utilize the network-theoretic framework to study unsteady fluid flows. Such analysis emphasizes how a collection of vortices or flow structures influences each other through a causal point of view on a network structure. We believe that the present study can provide an alternative tool to analyze how vortices or flow structures interact in the flow field and support the development of interaction-based models to capture unsteady vortex dynamics or turbulence.

In what follows, we report the work performed in three broad areas concerned with modeling unsteady fluid flows using network analysis. First, we introduce the framework of network theory in preparation to apply to the analysis of unsteady fluid flows. We then consider three canonical fluid flow problems:

1. discrete vortex interactions captured with sparsified-dynamics model;
2. energy transfer in modal network of fluid flow; and
3. network-based characterization of two-dimensional turbulence.

The report concludes with some remarks.

### 1.3 Network-Theoretic Framework

A network is defined by a collection of vertices joined by edges. These edges form the bonds that connect the vertices or the various entities of the system together. The edges can be associated with weights describing the importance of the connections between the vertices. Such a graph is called as a weighted graph. If the edges of the graph have an associated directivity (i.e., one vertex influences the other but not vice versa), the graph is called a directed graph. If a vertex influences itself, a self-loop edge (edge reconnected to itself) can represent such an effect. Any undirected graph  $\mathcal{G}$  can be described by a set of vertices  $V = \{v_1, v_2, \dots, v_N\}$ , a set of edges  $E$ , and a set of weights  $w$  associated with the edges, i.e.,  $\mathcal{G} = \{V, E, w\}$  [16, 2]. An example of a weighted graph is shown in Fig. 1 (left) with weights associated with the edges displayed. A complete graph  $\mathcal{K}_N$  with  $N = 5$ , shown in Fig. 1 (right), has all the vertices connected to each other. In other words, this graph has  $N$  vertices with complete set of possible  $N(N - 1)/2$  edges without any self-loops. We later use a weighted version of the complete graph to describe the interactions amongst a set of discrete point vortices in the context of fluid dynamics.

Network connections can be summarized by its adjacency matrix  $\mathbf{A}_{\mathcal{G}} \in \mathbb{R}^{N \times N}$ , which is given

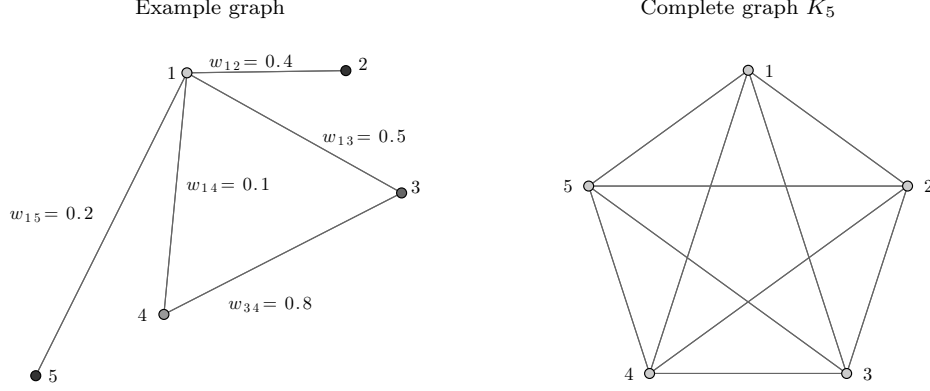


**Figure 1:** (left) An example weighted graph; and (right) a complete graph  $K_5$ .

by

$$[\mathbf{A}_{\mathcal{G}}]_{ij} = \begin{cases} w_{ij} & \text{if } (i, j) \in E \\ 0 & \text{otherwise.} \end{cases} \quad (1)$$

In an unweighted graph, the weight is set to unity if  $(i, j) \in E$ . The diagonal entries of the adjacency matrix relate to the weight of the self-connecting (loops) edges. The adjacency matrix of an undirected graph is symmetric. The degree  $k_i$  of a vertex  $i$  represents the summation of the weights of the edges connected to it given by  $k_i = \sum_{j=1}^N [\mathbf{A}_{\mathcal{G}}]_{ij}$ . The adjacency matrix for an example graph  $\mathbf{A}_{\mathcal{G}}$  and the complete graph  $\mathbf{A}_{K_5}$  shown in Fig. 1 are given by

$$\mathbf{A}_{\mathcal{G}} = \begin{pmatrix} 0 & 0.4 & 0.5 & 0.1 & 0.2 \\ 0.4 & 0 & 0 & 0 & 0 \\ 0.5 & 0 & 0 & 0.8 & 0 \\ 0.1 & 0 & 0.8 & 0 & 0 \\ 0.2 & 0 & 0 & 0 & 0 \end{pmatrix} \quad \text{and} \quad \mathbf{A}_{K_5} = \begin{pmatrix} 0 & 1 & 1 & 1 & 1 \\ 1 & 0 & 1 & 1 & 1 \\ 1 & 1 & 0 & 1 & 1 \\ 1 & 1 & 1 & 0 & 1 \\ 1 & 1 & 1 & 1 & 0 \end{pmatrix},$$

where  $\mathcal{G}$  is a weighted graph and  $K_5$  is an unweighted complete graph.

Another important matrix in graph theory is the graph Laplacian matrix  $\mathbf{L}_{\mathcal{G}} \in \mathbb{R}^{N \times N}$ , which is given by

$$[\mathbf{L}_{\mathcal{G}}]_{ij} = \begin{cases} k_i & \text{if } (i, j) \in E \text{ and } (i = j) \\ -w_{ij} & \text{if } (i, j) \in E \text{ and } (i \neq j) \\ 0 & \text{otherwise.} \end{cases} \quad (2)$$

The graph Laplacian matrix can also be deduced from the adjacency matrix,  $\mathbf{L}_{\mathcal{G}} = \mathbf{D}_{\mathcal{G}} - \mathbf{A}_{\mathcal{G}}$ , where  $\mathbf{D}_{\mathcal{G}} \in \mathbb{R}^{N \times N}$  is a diagonal matrix with elements equal to degrees of vertices,  $\mathbf{D}_{\mathcal{G}} = \text{diag}([k_i]_{i=1}^N)$ . For undirected networks, it is symmetric and positive semidefinite (singular). This Laplacian matrix is a discrete analog of the negative continuous Laplacian operator  $(-\nabla^2)$  and is also called as the discrete Laplacian. It is naturally defined by its quadratic form. If we have a linear system of the form  $\mathbf{L}_{\mathcal{G}} \mathbf{x} = \mathbf{b}$ , for the vector  $\mathbf{x} \in \mathbb{R}^N$ , the Laplacian quadratic form of a weighted graph  $\mathcal{G}$  is given by [17]

$$\mathbf{x}^T \mathbf{L}_{\mathcal{G}} \mathbf{x} = \sum_{(i,j) \in E} w_{ij} (x_i - x_j)^2. \quad (3)$$

The discrete Laplacian is a smoothness indicator of  $\mathbf{x}$  over the edges in  $\mathcal{G}$ . The Laplacian quadratic form becomes large as  $\mathbf{x}$  jumps over the edges of  $\mathcal{G}$ . The definitions of adjacency matrix and graph Laplacian form the building blocks of the graph-theoretic framework. The Laplacian quadratic form will be used below to introduce the notion of spectral similarity of graphs and graph sparsification.



## 2 Network Representation of Discrete Vortex Interactions

We apply network analysis to study the dynamics of a collection of point vortices [18, 19]. In the present work, the flow is assumed to be two-dimensional, incompressible, and inviscid. The spatial domain  $\mathcal{D}$  is taken to be infinitely large and the position of the vortices in the flow field is denoted by  $\mathbf{r} = (x, y) \in \mathcal{D}$ . We consider a collection of  $N$  vortices to be in the domain  $\mathcal{D}$  resulting in the vorticity field of

$$\omega(\mathbf{r}) = \sum_{j=1}^N \frac{\kappa_j}{2\pi} \delta(\mathbf{r} - \mathbf{r}_j), \quad (4)$$

where  $\kappa_j$  and  $\mathbf{r}_j$  are the strength (circulation) and position of the  $j$ -th vortex, respectively, and  $\delta(\cdot)$  is the Dirac delta function. The motion of the vortices is described by the Biot–Savart law

$$\frac{d\mathbf{r}_i}{dt} = \sum_{\substack{j=1 \\ j \neq i}}^N \frac{\kappa_j}{2\pi} \frac{\hat{\mathbf{k}} \times (\mathbf{r}_i - \mathbf{r}_j)}{|\mathbf{r}_i - \mathbf{r}_j|^2}, \quad (5)$$

where  $\hat{\mathbf{k}}$  is the out-of-plane unit normal vector. To determine the trajectories of the vortices, we numerically integrate the above equation. This equation is the basis of the discrete vortex methods that are used to simulate unsteady vortical flows in place of discretizing the two-dimensional Euler equations.

The objective of the present work is to describe the interactions amongst a set of point vortices with graph theory and network analysis. The dynamics of the vortices will be modeled on a sparsified graph in place of the full (complete) graph to derive a sparsified model that accurately captures the motion of the vortices while conserving physical properties, such as circulation, Hamiltonian, as well as linear and angular impulse.

### 2.1 Representing Vortex Interactions on a Graph

A vortex is advected by the induced velocity from the other vortices and not by its own velocity as seen in equation (5). Each vortex is influenced by all other vortices, which means that each and every vortex has a connection to all other vortices without any self-loops. Thus, the discrete system of  $N$  point vortices can be represented by a weighted complete graph,  $\mathcal{K}_N$ . The vertices or nodes of the graph represent the discrete point vortices and the edge weights represent the strength of the connections between them.

The motion of point vortices is influenced by the strengths (circulation) of the individual point vortices and the distances between them. The shorter the distance between the point vortices, the higher is the influence of the vortices on each other. Also, a vortex with higher strength has more ability to influence the surrounding vortices compared to that with lower strength. We assign the weight for the interaction between two vortices to be dependent on the characteristic vortex induced velocity based on the strengths of the two vortices and the distance between them. Thus, this implies that the edge weight for the vortex network should be proportional to  $\kappa/r$ , where  $\kappa$  is the characteristic strength of the two vortices and  $r$  is the distance between them within the network.

The distance between the vortices is dependent on the location of the two point vortices  $|\mathbf{r}_i - \mathbf{r}_j|$  and the characteristic strength can be established by considering their geometric mean  $\sqrt{|\kappa_i \kappa_j|}$ . This choice makes the adjacency matrix symmetric which allows the use of the spectral sparsification algorithm discussed in §2.2. Therefore, the adjacency matrix for the graph representation of a set

of point vortices can be defined as,

$$[\mathbf{A}_{\mathcal{G}}]_{ij} = \begin{cases} \frac{\sqrt{|\kappa_i \kappa_j|}}{|\mathbf{r}_i - \mathbf{r}_j|} & \text{if } (i, j) \in E \text{ and } i \neq j \\ 0 & \text{otherwise.} \end{cases} \quad (6)$$

Note that the diagonal elements of the adjacency matrix are zero as the self-induced velocity components are zero. This translates to the graph not having any self-loops. The interaction between the system of discrete point vortices represented on a complete graph can be sparsified for deriving the sparse vortex interaction model.

In addition to considering the geometric mean of the circulation for the weights, algebraic mean of the circulation was also considered. The computation using the algebraic mean (i.e.,  $\frac{1}{2}(|\kappa_i| + |\kappa_j|)/|\mathbf{r}_i - \mathbf{r}_j|$ ) for the weights perform similar to that with the above geometric mean. While we show that geometric mean sufficiently captures the vortex interaction, there may be some room for optimizing the choice of weights. In what follows we utilize the geometric mean in equation (25) for the network weight.

## 2.2 Spectral Sparsification

The sparse approximation of dense graphs can provide numerous benefits for numerical computation. Graph sparsification is useful for designing computationally efficient algorithms and helps in identifying representative edges and associated weights [20]. Graph similarity, which forms the basis for graph sparsification, can be derived in a number of ways depending on the desired similarity properties. Distance similarity of graphs [21] can be achieved by sparse graphs called spanners that keep the same shortest-path distance between each pair of vertices as in the original graph while cut similarity [22] can be achieved by maintaining the weight of the edges leaving a set of vertices of the sparse graph to be the same as that of the original graph. A much stronger notion of similarity referred to as *spectral similarity* was introduced by [20]. Spectral similarity is closely tied to the Laplacian quadratic form of the graphs as defined by equation (3). The concept of spectral similarity directly leads to spectral sparsification of graphs; that is to create sparse graphs, which are spectrally similar to the original graph.

Spectral sparsification is a more general abstraction than cut sparsifiers and maintains spectral similarity between the sparsified and original graphs. In particular, spectral sparsification can remove some of the edges in the graph, while maintaining similar adjacency and Laplacian eigen-spectra. One of the key features of spectral sparsification is that it keeps the sum of the weights leaving the vertex of a graph constant. A spectral sparsifier is a subgraph of the original graph whose Laplacian quadratic form is approximately the same as the original graph [20].

Sparsification involves the creation of a sparse graph  $\mathcal{G}_S$  from the original graph  $\mathcal{G}$  based on an approximation order of  $\epsilon$ . The quadratic form induced by graph Laplacian of  $\mathcal{G}$  is maintained up to a multiplicative  $(1 \pm \epsilon)$  factor by spectral sparsification [23]. Thus, the sparse graph  $\mathcal{G}_S$  is a  $(1 \pm \epsilon)$ -spectral approximation of  $\mathcal{G}$ . The approximation order  $\epsilon$  can vary from zero to unity. The approximation with  $\epsilon = 0$  indicates that  $\mathcal{G}_S$  is same as original graph  $\mathcal{G}$  and none of the edges are sparsified, while  $\epsilon = 1$  relaxes the quadratic form induced by the sparse graph to within twice of that induced by the original graph. An approximation of  $\epsilon = 1$  leads to a heavily sparsified graph. Denoting the Laplacian matrices of  $\mathcal{G}$  and  $\mathcal{G}_S$  by  $\mathbf{L}_{\mathcal{G}}$  and  $\mathbf{L}_{\mathcal{G}_S}$ , respectively, the spectrally sparsified Laplacian satisfies

$$(1 - \epsilon)\mathbf{x}^T \mathbf{L}_{\mathcal{G}} \mathbf{x} \leq \mathbf{x}^T \mathbf{L}_{\mathcal{G}_S} \mathbf{x} \leq (1 + \epsilon)\mathbf{x}^T \mathbf{L}_{\mathcal{G}} \mathbf{x} \quad (7)$$

at least with probability  $1/2$  with large  $N$  for all  $\mathbf{x} \in \mathbb{R}^N$  [24]. For the example problem considered later, these bounds are much tighter. This tells us that  $\mathbf{L}_{\mathcal{G}_S}$  holds eigenvalues similar to those of

$\mathbf{L}_{\mathcal{G}}$ . These spectrally similar sparse graphs are found using the spectral sparsification algorithm based on sampling by effective resistance discussed below.

Before we discuss how a graph can be sparsified, let us first follow the works of [1] and [25] to establish an analogy of a graph to an electrical circuit. If the entire graph is viewed as a resistive circuit, we can define a resistance on the individual edges  $e = (i, j)$  of the graph. According to Thomson's principle, the potentials and currents in a resistive circuit distribute themselves so as to minimize the total energy in the network [1]. This energy minimization principle leads to the concept of effective resistance.

Effective resistance between vertices  $i$  and  $j$  is the potential difference induced between them when a unit current is injected at one vertex and extracted at the other [1, 25]. The effective graph resistance (also called as resistance distance) is the sum of the effective resistance over all the pairs of vertices in the graph  $\mathcal{G}$  [26, 27]. Rayleigh's monotonicity law states that pairwise effective resistance is a non-increasing function of the edge weights [28].

In order to obtain an expression of effective resistance for graph sparsification, we orient the edges of the original weighted undirected graph  $\mathcal{G}$  with  $N$  vertices and  $M$  edges. We can represent any directed graph by a signed edge ( $e$ )-vertex ( $v$ ) incidence matrix  $\mathbf{B}_{\mathcal{G}} \in \mathbb{R}^{M \times N}$  given by

$$[\mathbf{B}_{\mathcal{G}}]_{ev} = \begin{cases} 1 & \text{if } e \in E \text{ and } v \text{ is the head of } e \\ -1 & \text{if } e \in E \text{ and } v \text{ is the tail of } e \\ 0 & \text{otherwise.} \end{cases} \quad (8)$$

The row of  $\mathbf{B}_{\mathcal{G}}$  corresponding to an edge  $e = (i, j)$  is given by  $(\mathbf{p}_i - \mathbf{q}_j)$ , where  $\mathbf{p}_i$  and  $\mathbf{q}_j$  are elementary unit vectors in the  $i$  and  $j$  directions, respectively. If the edge weights of the graph are represented in a diagonal matrix given by  $\mathbf{C}_{\mathcal{G}} \in \mathbb{R}^{M \times M}$ , we can express the Laplacian matrix based on the incidence matrix as

$$\mathbf{L}_{\mathcal{G}} = \mathbf{B}_{\mathcal{G}}^T \mathbf{C}_{\mathcal{G}} \mathbf{B}_{\mathcal{G}} = \sum_{i,j \in E} w_{ij} (\mathbf{p}_i - \mathbf{q}_j)(\mathbf{p}_i - \mathbf{q}_j)^T. \quad (9)$$

The above relation holds true only for undirected graphs.

For an edge corresponding to  $e = (i, j)$ , the unit current is injected at vertex  $i$  and extracted at vertex  $j$ . Thus, we set the electrical current across the edge to be  $(\mathbf{p}_i - \mathbf{q}_j)$ . The potential induced by this current at the vertices is given by  $\mathbf{L}_{\mathcal{G}}^+(\mathbf{p}_i - \mathbf{q}_j)$ , where  $\mathbf{L}_{\mathcal{G}}^+$  is the Moore-Penrose pseudoinverse of the Laplacian matrix  $\mathbf{L}_{\mathcal{G}}$  [25]. The potential difference across edge  $e = (i, j)$  is then given by  $(\mathbf{p}_i - \mathbf{q}_j)^T \mathbf{L}_{\mathcal{G}}^+(\mathbf{p}_i - \mathbf{q}_j)$ . Thus, for unit current, the effective resistance across edge  $e = (i, j)$  which corresponds to the potential difference can be expressed as

$$[R_e]_{ij} = (\mathbf{p}_i - \mathbf{q}_j)^T \mathbf{L}_{\mathcal{G}}^+(\mathbf{p}_i - \mathbf{q}_j). \quad (10)$$

The above expression is used for computing effective resistance of the edges of the graph. The sparsification of the original graph  $\mathcal{G} = \{V, E, w\}$  is performed with an algorithm **Sparsify** [24] to produce a sparse graph  $\mathcal{G}_S = \{V, \tilde{E}, \tilde{w}\}$  where  $\tilde{w}$  are the weights corresponding to the sparse graph  $\mathcal{G}_S$ . This algorithm is based on the concept of effective resistance and yields a  $(1 + \epsilon)$  sparse graph  $\mathcal{G}_S$ . This sparse graph contains a reduced number of  $\mathcal{O}(N \log(N)/\epsilon^2)$  edges. The procedure for sparsification  $\mathcal{G}_S = \text{Sparsify}(\mathcal{G})$  is summarized below.

We first create a list of the edges  $E$  with the associated weights of the original graph  $\mathcal{G}$ . The adjacency and Laplacian matrices of graph  $\mathcal{G}$  are constructed from equations (1) and (2). The

Moore–Penrose pseudoinverse of the Laplacian matrix  $\mathbf{L}_{\mathcal{G}}^+$  is then computed. For each edge in the edge list, the elementary unit vectors,  $\mathbf{p}_i$  and  $\mathbf{q}_j$ , and edge weights  $w_e$  are obtained. Next, the effective resistance  $[R_e]_{ij}$  corresponding to each edge is computed from equation (10).

A random edge  $e = (i, j)$  from the edge list of graph  $\mathcal{G}$  is chosen with probability  $p_e$  proportional to  $w_e[R_e]_{ij}$ . The edge  $e$  is added to the sparse graph  $\mathcal{G}_S$  with the weight given by  $\tilde{w}_e = w_e/qp_e$ , where  $q = 8N \log_2(N)/\epsilon^2$ . We take integer( $q$ ) number of samples independently without replacement and sum the weights if an edge is chosen more than once. The resulting graph becomes the sparsified graph  $\mathcal{G}_S$  that satisfies equation (7) with eigenvalues similar to those of  $\mathcal{G}$ .

After the random sampling procedure, a sparsified adjacency matrix  $\mathbf{A}_{\mathcal{G}_S}$  is obtained. For convenience, we define the ratio of the sparsified and original adjacency matrix weights as  $W_{ij}$ ,

$$W_{ij} \equiv \begin{cases} \tilde{w}_{ij}/w_{ij} & \text{if } (i, j) \in \tilde{E} \\ 0 & \text{otherwise.} \end{cases} \quad (11)$$

This sparsification factor  $W_{ij}$  is related to the probability of an edge  $e = (i, j)$  of graph  $\mathcal{G}$  being sampled. The edges of the original graph that are not sampled during the random sampling procedure have zero weights in the sparsified graph. These edges are cut during sparsification. The spectral sparsification procedure also redistributes the weights of the cut edges among the other edges of the sparsified graph. Thus, cutting of graph edges is compensated by redistribution of the weights to preserve spectral properties of the original graph.

The spectral sparsification algorithm described above produces a  $(1 \pm \epsilon)$  expander graph, i.e., sparsifier with strong connectivity properties when  $\epsilon \geq 1/\sqrt{N}$ , where  $N$  is the number of vertices [24]. With the concept of graphs and spectral sparsification now discussed, we consider the application of network analysis to discrete vortex dynamics in the next section.

## 2.3 Sparsification of Vortex Interactions

In this section, we construct sparsified representation of vortex interactions by sparsifying and redistributing the weights of the connections between the point vortices as discussed in §2.2. We consider a configuration of  $N$  point vortices in  $n_c$  clusters. This setup allows us to examine the effect of sparsification on a cluster of vortices. The edge weights represented in the adjacency matrix are given by equation (25).

Let us first consider a collection of  $N = 100$  point vortices with  $n_c = 5$  with each cluster containing 20 vortices. The clusters in this setup can be clearly identified by the use of graph clustering algorithms. An algorithm maximizing modularity [29] can be utilized for the identification of clusters. One could also use  $k$ -means for cluster identification similar to the work performed by [30]. The point vortices in a particular cluster are given a normal distribution in space with a radial standard deviation of  $\sigma_r = 0.2$ . The strength of the point vortices,  $\kappa_i$ , within the individual clusters have a normal distribution with the mean of  $\bar{\kappa} = 0.1$  and a standard deviation of  $\sigma_{\kappa} = 0.01$ . The setup for this configuration is shown in figure 2. The positions of the clusters are normalized by the average radial distance of the centroid of the clusters from the geometric center of the system ( $R_o$ ).

The original point vortex distribution modeled as a complete graph is shown in figure 3 (top left). The colors of the point vortices (network vertices) indicate their unweighted degree (number of edge connections). As the original graph here is a complete graph  $\mathcal{K}_N$ , each vortex is connected to every other vortex. Thus, the unweighted degree of each vortex in this example is  $N - 1 = 99$ . The sparsity pattern of the adjacency matrix for the complete graph  $\mathbf{A}_{\mathcal{K}_N}$  is shown in figure 3 (top right). We also note in the figure the sparsity index  $S$ , defined as  $S \equiv n_{\text{non-zero}}/N^2$  with  $n_{\text{non-zero}}$  being the number of non-zero weights in the adjacency matrix and  $N$  being the number of vortices.

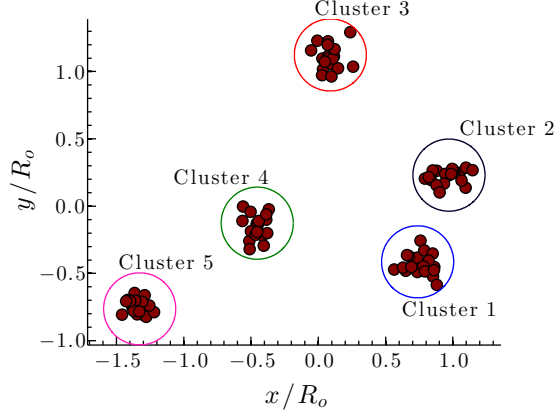


**Figure 2:** The spatial arrangement of  $N = 100$  point vortices with five clusters.

As the diagonal elements of the adjacency matrix have zero weights,  $n_{\text{non-zero}} = N(N - 1)$  for the complete graph. For  $N = 100$ , a sparsity index of  $S = 0.99$  is obtained for the original graph.

We now perform spectral sparsification on the original graph ( $\mathcal{G} = \mathcal{K}_N$ ) using the algorithm  $\mathcal{G}_S = \text{Sparsify}(\mathcal{G})$  described in §2.2 to obtain the spectrally similar sparse representations of the complete graph based on approximation order  $\epsilon$ . The corresponding adjacency matrix,  $\mathbf{A}_{\mathcal{G}_S}$  can also be found. The vortex network for sparse graph and the sparsity pattern of  $\mathbf{A}_{\mathcal{G}_S}$  corresponding to approximation order of  $\epsilon = 0.5$  are shown in Fig. 3 (middle). We observe that the number of edges (connections) between the vortices in cluster 3 and 5 are reduced. Because the weights of the adjacency matrix are inversely proportional to the distance between the vortices, a large number of edges between the vortices of the clusters with larger distances are cut during sparsification. The sparsity index decreases from  $S = 0.99$  for the original complete graph to  $S = 0.741$  for the sparse graph ( $\epsilon = 0.5$ ), reducing the number of connections by approximately 25 percent.

The vortex network and sparsity patterns for approximation order of  $\epsilon = 1$  are shown in figure 3 (bottom). We observe dense representation of the connections between the clusters 1 and 2. Thus, the proximity in clusters is identified both in the network structure and the sparsity patterns. Also, we realize from the sparsity patterns that the connections between the vortices in a particular cluster are maintained while majority of the inter-cluster ties are cut resulting in a sparse graph. The number of connections in the sparse graph for  $\epsilon = 1$  are reduced dramatically by nearly 60 percent with  $S = 0.4006$ .

For weighted graphs, the effective resistance is computed in such a way so as to maintain spectral similarity. The eigenspectra ( $\sigma$  and  $\lambda$ ) of the adjacency and Laplacian matrices for the sparse and original graphs are compared in figure 4. We observe from figure 4 that the spectra of the sparse and original configurations are in good agreement as expected. The second smallest eigenvalue of the Laplacian matrix represents the spectral gap or algebraic connectivity of the graph, i.e., vertices connected by at least a single path [2]. As observed from Fig. 4, the spectral gap is greater than zero for original and sparse graphs indicating that the graph is connected. Thus, sparsification preserves the connectivity properties of the original graph. The sparsified graphs slightly underpredict the maximum eigenvalues of the adjacency and Laplacian matrices compared to the original graph. The preservation of spectral properties is attractive if the sparsified network is to be used to describe the dynamics of the vortices. We expect the overall motion of the vortices to remain similar with sparsified representations of the vortex interactions.

Sparsification helps identify the individual clusters by creating subgraphs within a graph where the density of the edges between vertices is much greater than that outside it. The spectral

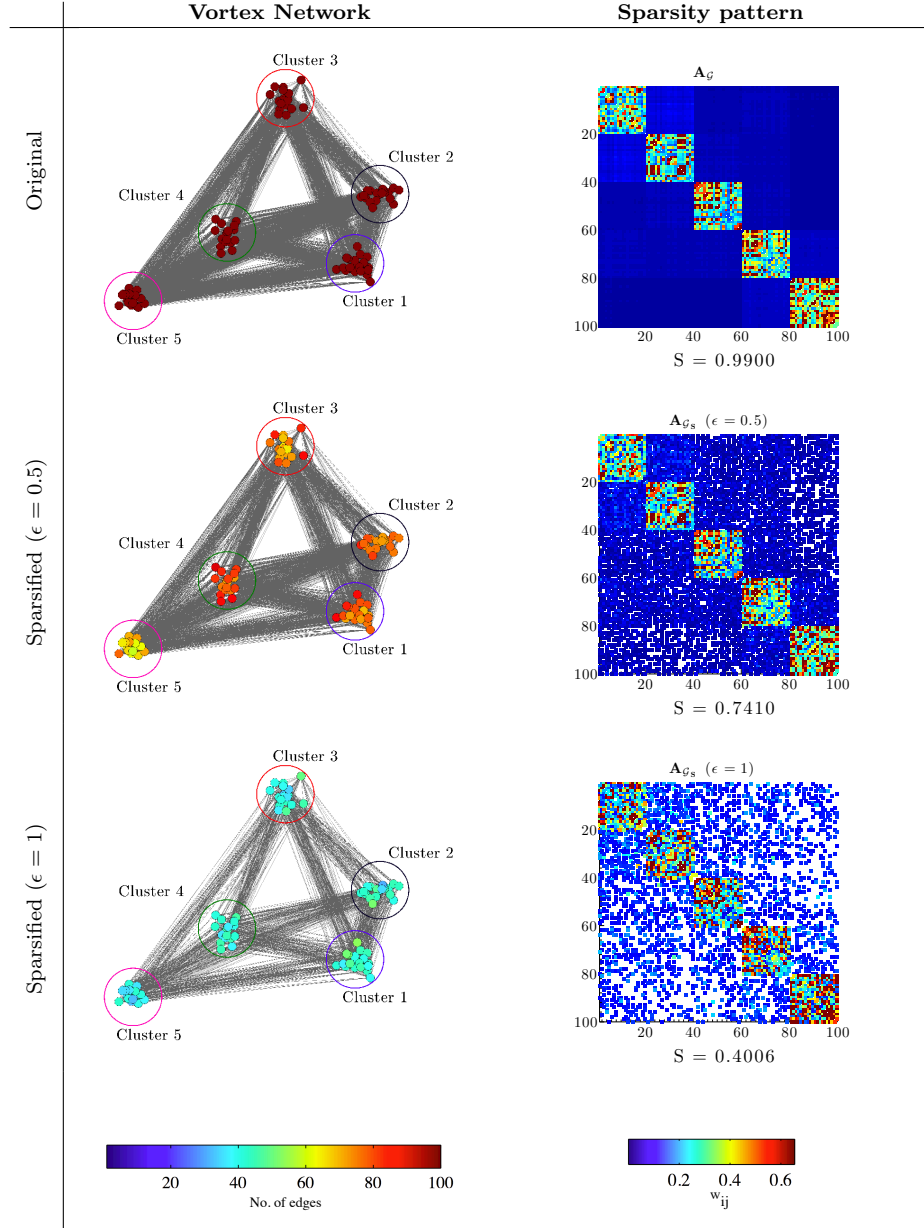


**Figure 3:** Original and sparsified graphs and their respective sparsity patterns of the adjacency matrix for  $N = 100$  vortices. The color of the nodes of the vortex network represents the unweighted connections (number of connected edges) of the individual point vortices. The color in the sparsity patterns of the adjacency matrix indicates the adjacency weights  $w_{ij}$  for original graph  $A_G$  and  $\tilde{w}_{ij}$  for sparse graphs  $A_{G_S}$ . The empty white spaces indicate sparsity in the adjacency matrix. Sparsity index is  $S \equiv n_{\text{non-zero}}/N^2$ , where  $n_{\text{non-zero}}$  is the number of non-zero weights (elements) in adjacency matrix and  $N$  is the number of vortices. The colored circles in the vortex network represent the individual cluster groups.

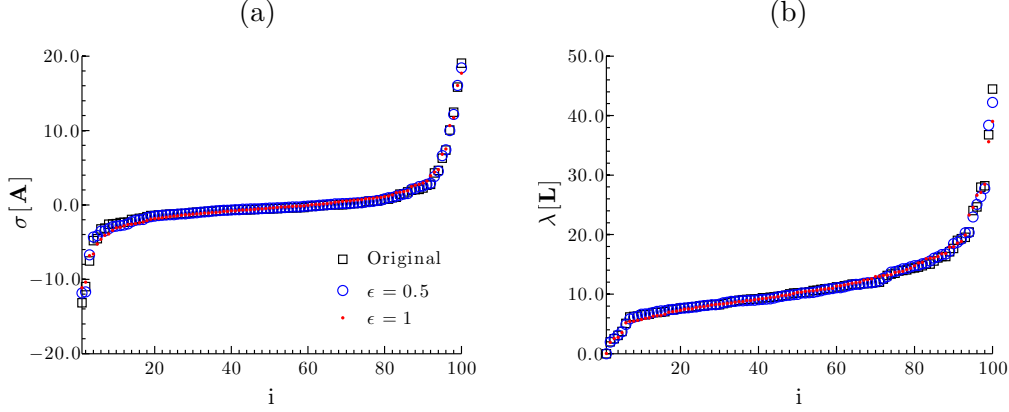


**Figure 4:** Eigenvalue spectra of (a) adjacency and (b) Laplacian matrices of the sparsified graphs with  $\epsilon = 0.5$  and 1 in comparison to the original graph.

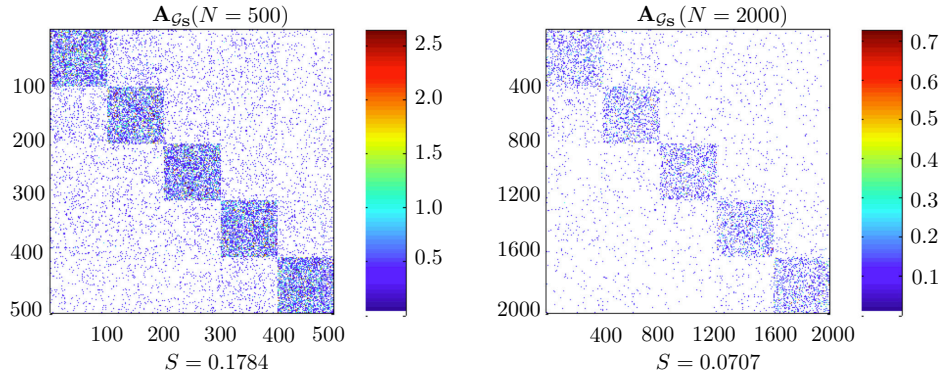


**Figure 5:** Sparsity patterns of adjacency matrix for  $N = 500$  and 2000 for approximation order  $\epsilon = 1$ . The color in the sparsity patterns of the adjacency matrix denotes the adjacency weights  $\tilde{w}_{ij}$  with the empty white space indicating sparsity.

sparsification procedure leads to the reduction in the number of edges to  $\mathcal{O}(N \log(N)/\epsilon^2)$  for large  $N$ . We examine the performance of spectral sparsification on the current example for increasing the total number of vortices. As in the example that was previously considered, we maintain a constant number of clusters  $n_c = 5$  but increase the number of vortices in each cluster  $N/n_c$ . The sparsity patterns of the adjacency matrix for  $N = 500$  and 2000 with approximation order  $\epsilon = 1$  are shown in Fig. 5. We observe that as the number of vortices increases, the adjacency matrix of the sparsified graph becomes increasingly sparse. Similar to the case with  $N = 100$  vortices, the majority of the ties within a cluster are maintained while a large number of inter-cluster ties are cut. The sparsity index decreases from  $S = 0.1784$  to 0.0707 for  $N = 500$  to 2000, which is a substantial amount of sparsification. Let us further show the sparsity index  $S$  for increasing  $N$  with different approximation order  $\epsilon$  in Fig. 6. The sparsity index  $S$  decreases with an increase in  $\epsilon$  and the number of vortices. The expected behavior of the sparsity index  $S = \mathcal{O}(N \log(N))/(N^2) = \mathcal{O}(\log(N)/N)$  is observed for larger  $N$ . The trend deviates from the expected behavior for lower  $N$  as the availability of the connections for redistribution of the weights of the sparsified connections decreases.

We observe that the sparsification algorithm provides us with a heavily sparsified model to produce a computationally tractable representation of the vortex-to-vortex interaction. We further

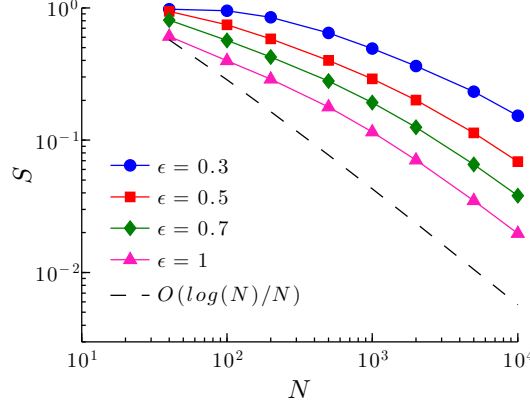


**Figure 6:** Variation of sparsity index  $S$  for sparsification with increasing number of point vortices. The reference black line represents  $\log(N)/N$ .

note that the sparsification algorithm can be easily parallelized, which is attractive to further reduce the computational wait time. The bulk motion of clusters of point vortices could be tracked effectively by tracking their individual centroids. The present approach may lead to algorithms similar to fast particle summation methods where near and far-field effects are taken into consideration [31].

## 2.4 Sparsified-Dynamics Model

The sparsified vortex interactions can be used for analyzing the dynamics of the system of discrete point vortices. Spectral sparsification can be viewed as adjusting the strength of the vortices in the Biot-Savart law through the sparsification factor  $W$  given by equation (11). We can incorporate the weights of the sparse graph into the Biot-Savart law as

$$\frac{d\mathbf{r}_i}{dt} = \sum_{\substack{j=1 \\ W_{ij} \neq 0}}^N W_{ij} \frac{\kappa_j}{2\pi} \frac{\hat{\mathbf{k}} \times (\mathbf{r}_i - \mathbf{r}_j)}{|\mathbf{r}_i - \mathbf{r}_j|^2}, \quad (12)$$

where  $W_{ij}$  is the sparsification factor. The above expression significantly reduces the amount of computation compared to the original Biot-Savart law, because the sparsification has made a significant number of elements of  $W$  to be zero, as seen in figures 3 and 5.

For evaluating the effect of sparsification on dynamics of the point vortices, we consider the same example presented in §2.3 with  $N = 100$  vortices as the initial condition. The objective here is to accurately capture the dynamics of the vortex clusters with the sparsified Biot-Savart law given by equation (12). The bulk motions of the clusters of point vortices are well represented by the centroid of the individual clusters. The original and the sparsified dynamics are given by equations (5) and (12), respectively, and are integrated in time with the fourth-order Runge-Kutta method. The results from the sparsified-dynamics model are shown in figures 7 and 8.

For the present analysis, time is non-dimensionalized by considering the cumulative circulation of the vortices of the cluster ( $\Gamma$ ) and average radial distance of the centroid of the clusters from the geometric center of the overall system at the initial time ( $R_o$ ). As the advective velocity of an isolated cluster of point vortices of strength  $\Gamma$  at  $R_o$  is given by  $u^* = \Gamma/2\pi R_o$ , the non-dimensional time can be deduced as  $tu^*/R_o = t\Gamma/2\pi R_o^2$ . In the current example, each individual cluster has a collection of vortices with their strength having a mean of  $\bar{\kappa} = 0.1$  (with a normal distribution).



Thus, for  $n$  vortices in a cluster,  $\Gamma = n\bar{\kappa}$ . The error in position of the centroid of the clusters for the sparsified setting with respect to the original setting given by  $|\mathbf{r}_\epsilon - \mathbf{r}|$  is non-dimensionalized by the average radial distance of the centroid of the clusters from the geometric center of the system at the initial time ( $R_o$ ).

Let us consider the case where sparsification is performed only once to determine the sparsification factor  $W_{ij}$  before initiating the time integration. The same sparsification factor is used throughout the time integration. This procedure is inexpensive as sparsification is performed only once *a priori*. The trace of the positions of the centroid of the individual clusters and their error for approximation orders of  $\epsilon = 0.5$  and 1 for a single sparsification are shown in figures 7 (top) and 8 (top), respectively. Considering the number of connections cut between the vortices for sparse approximations, the trajectories of the centroid of the clusters based on sparse vortex dynamics agrees reasonably with those from full dynamics. On comparing the errors, we find that the errors with approximation order of  $\epsilon = 0.5$  is less than those with  $\epsilon = 1$ , which is expected. Despite the Biot–Savart law being nonlinear, the present sparsified approach achieves a reasonable agreement with the full nonlinear solution.

If the clusters of vortices are far from each other, the connections cut between their vortices do not cause a large change in the dynamics while the connections cut between clusters close to each other affect the dynamics considerably. As time progresses, the relative distance between vortices change, resulting in an increase in error. For  $t\Gamma/2\pi R_o^2 > 1$ , we observe that the errors in sparse vortex dynamics increases to  $\approx 0.5R_o$ . As the adjacency weights  $w_{ij}$  and the sparsification factor  $W_{ij}$  are based on the initial position of the vortices, the ratio does not hold over large times. This calls for adjustment of the weights and periodic sparsification to adapt to the dynamically changing position of the vortices.

We thus consider resparsification of the graph representing the system of point vortices periodically at  $(0.1t\Gamma/2\pi R_o^2)$  and  $(0.01t\Gamma/2\pi R_o^2)$  for both approximation orders. The trace of the centroids and error for approximation orders of  $\epsilon = 0.5$  and 1 with resparsification are shown in middle and bottom subfigures, respectively, of figures 7 and 8. We observe that the error decreases significantly with resparsification. The error in position reduces from  $\mathcal{O}(10^{-1})$  to  $\mathcal{O}(10^{-2})$  with resparsification. We notice that the centroid trajectories based on the sparse and original calculations become increasingly similar with resparsification. Resparsification updates the sparsification factor periodically based on the position and strength of the vortices and decreases the error by an order of magnitude. Thus, the nonlinear evolution of discrete vortex dynamics is well predicted by the sparsification techniques.

One of the advantages of sparsification is the decreased computational cost due to increased sparsity of the connections between the vortices. This could potentially lead to design of faster algorithms based on sparsification strategies. Let us first evaluate the offline cost of computing effective resistance and random sampling required for spectral sparsification. The time required for computing effective resistance  $t_r$  and time required for random sampling  $t_s$  is shown in figures 9(a) and (b) respectively. All computations were performed in MATLAB on an iMac with 3.4 GHz Intel Core i7 processor. We can observe that for each edge, the computation time of effective resistance is  $\mathcal{O}(\log(N))$ , hence requiring  $\mathcal{O}(N^2 \log(N))$  for the overall effective resistance computation. The random sampling procedure takes  $\mathcal{O}(N^2)$  time for all the approximation orders. We compare the computational time  $t_d$  required at each step of numerical integration of the Biot–Savart law for the original and sparse configuration. We can observe from figure 9(c) that the original configuration takes  $\mathcal{O}(N^2)$  time equivalent to the number of edges in the complete graph, while for the sparse configuration the computation time is reduced to  $\mathcal{O}(N \log(N))$ .

There is always a tradeoff amongst the level of sparsification, the error that appears in the dynamics, and the associated computational cost. The sparser the network is, the faster the com-

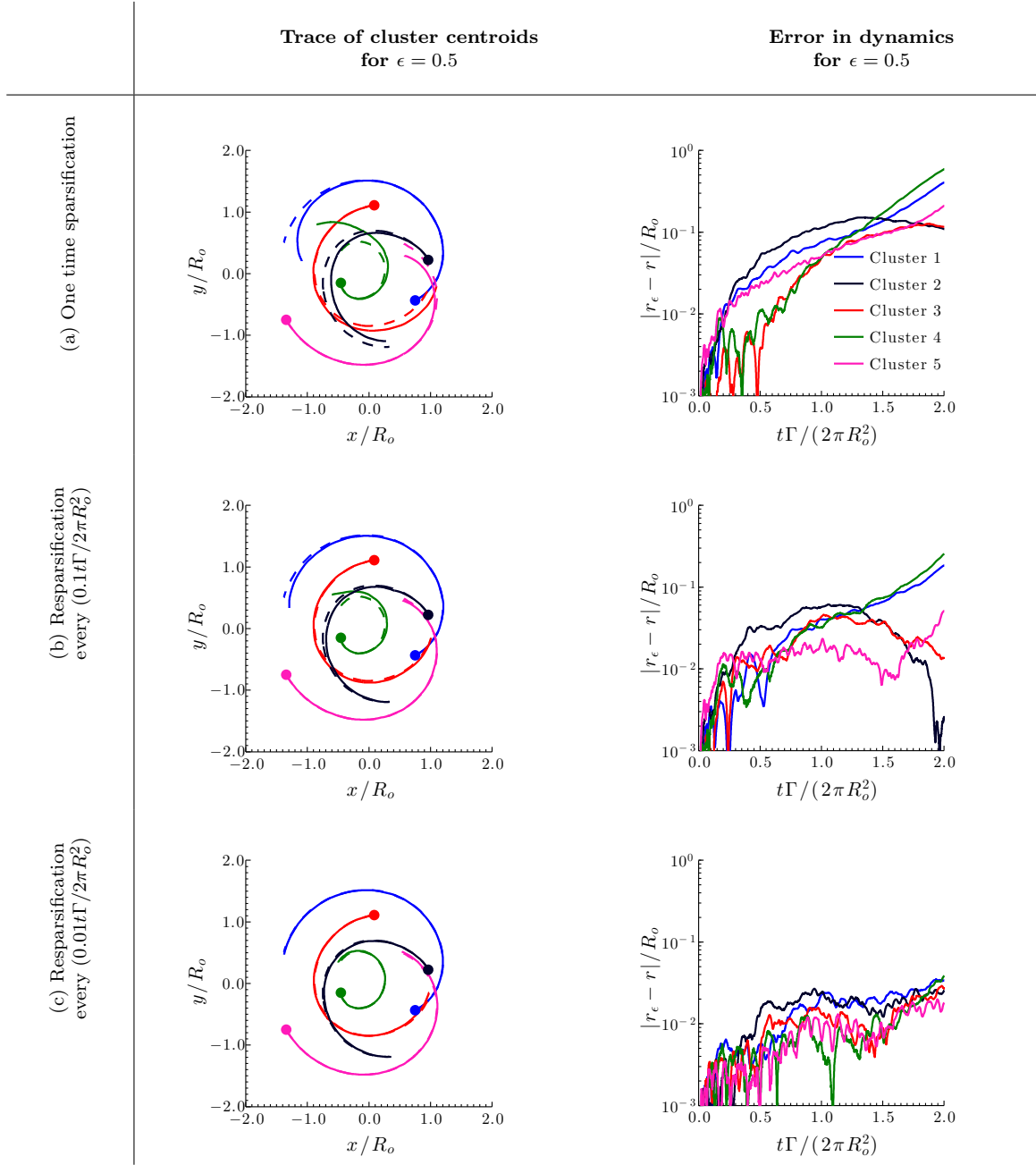


**Figure 7:** Trajectories of the centroids (left) and error in position of centroids (right) of the vortex clusters based on sparse graph ( $\epsilon = 0.5$ ) and original graph with time for  $N = 100, \bar{\kappa} = 0.1$ . (a) trajectories and error based on sparsification performed only at the initial step while (b) results based on resparsification performed at every  $(0.1t\Gamma/2\pi R_o^2)$  and (c) results based on resparsification performed at every  $(0.01t\Gamma/2\pi R_o^2)$ . The full nonlinear solution is shown with dashed lines.

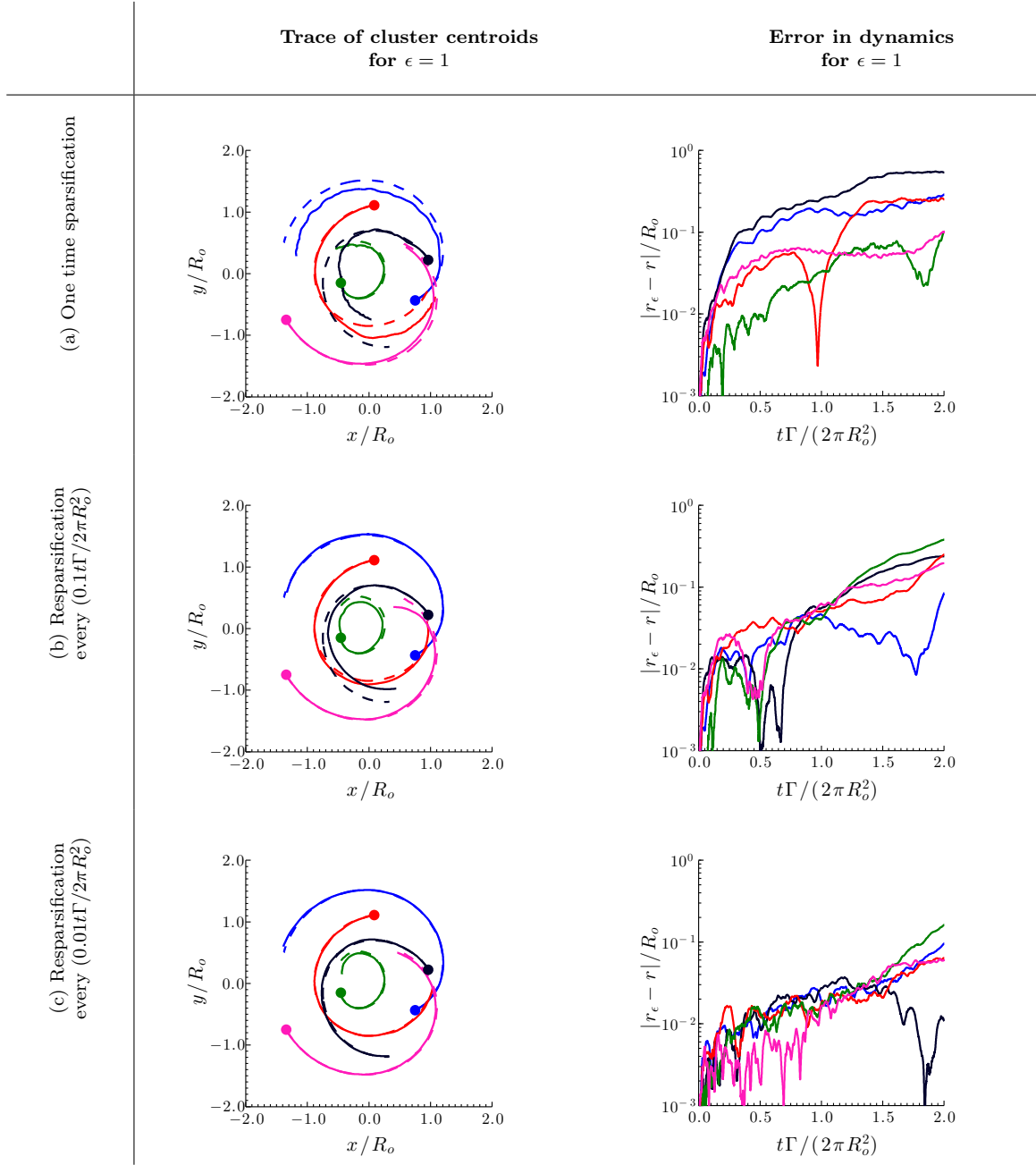


**Figure 8:** Trajectories of the centroids (left) and error in position of centroids (right) of the vortex clusters based on sparse graph ( $\epsilon = 1$ ) and original graph with time for  $N = 100, \bar{\kappa} = 0.1$ . (a) trajectories and error based on sparsification performed only at the initial step while (b) results based on resparsification performed at every  $(0.1t\Gamma/2\pi R_o^2)$  and (c) results based on resparsification performed at every  $(0.01t\Gamma/2\pi R_o^2)$ . The full nonlinear solution is shown with dashed lines.

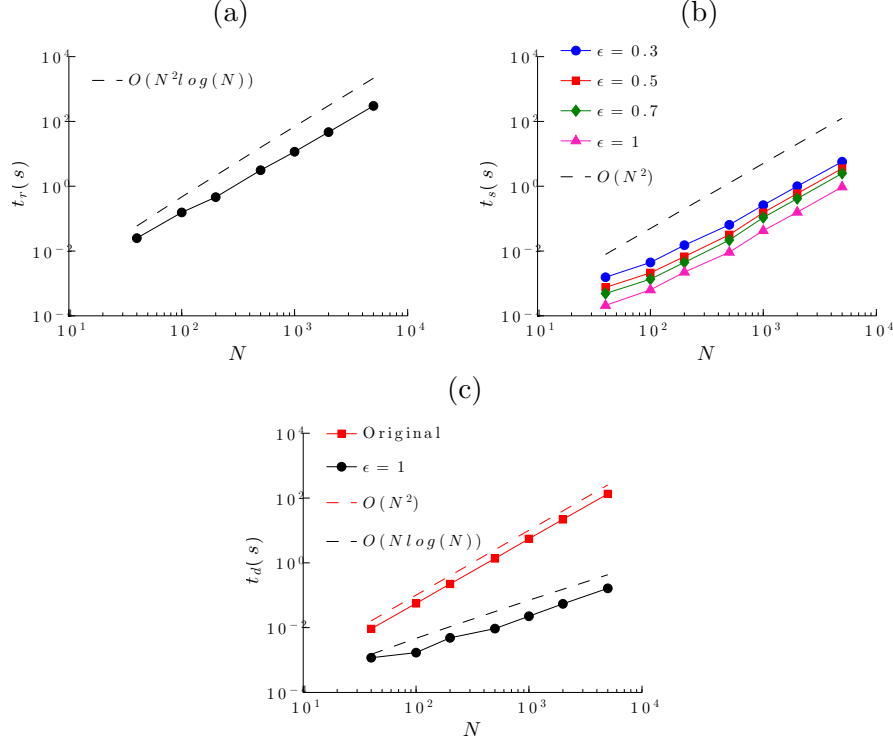


**Figure 9:** The time required for computation of (a) effective resistance and (b) random sampling for different approximation orders for one-time sparsification. The dashed lines indicate the expected trends. (c) Time required for numerical integration at each step for original and sparsified configuration with  $\epsilon = 1$ .

putation can become but may compromise accuracy. To increase the computational accuracy, resparsification can be performed but can introduce an additional computational load. We evaluate the computational cost for numerical integration until a total time of  $0.1t\Gamma/2\pi R_o^2$ . The time required for resparsification and numerical integration for the two different resparsification frequencies (performed every  $0.1t\Gamma/2\pi R_o^2$  and  $0.01t\Gamma/2\pi R_o^2$ ) considered in this work for original and sparse configuration with  $\epsilon = 1$  is shown in figure 10. It should be noted that for the resparsification performed every  $0.1t\Gamma/2\pi R_o^2$ , resparsification is performed once for the total time considered. For resparsification conducted every  $0.01t\Gamma/2\pi R_o^2$ , resparsification is performed ten times. We can see that the time required for resparsification at every  $0.1t\Gamma/2\pi R_o^2$  is considerably less compared to the original configuration. With increase in resparsification frequency, though the time required is less compared to the original configuration, there is increased cost associated with resparsification.

To illustrate that the trajectory prediction using sparsification cannot be performed naively, we compare the results from spectral sparsification with those based on random edge removal (without redistribution of edge weights). We keep the number of cuts identical to that achieved by spectral sparsification for fairness. The sparsity patterns for random cuts with sparsity  $S = 0.7410$  and  $0.4006$  and the corresponding Laplacian eigenspectra are shown in figure 11. We observe that the spectra from the randomly sparsified graphs grossly under-predicts that of the original graph.

The trace of the positions of the centroid of the individual clusters and their error for random cuts with sparsity  $S = 0.7410$  and  $0.4006$  for one-time sparsification are shown in figure 12. The random-cut approximation performs poorly as compared to spectral sparsification and the dynamics of the centroid of the vortex clusters are not captured. As the connections between the vortices are randomly cut, the centroids of the clusters move slower compared to the original configuration

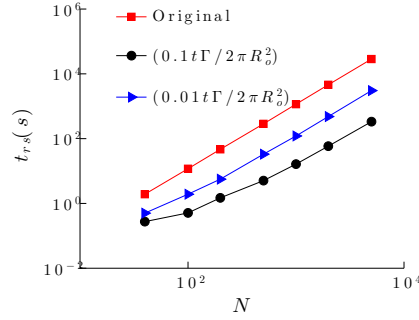


**Figure 10:** The time required for numerical integration for a total time of  $0.1t\Gamma/2\pi R_o^2$  with different resparsification frequencies.

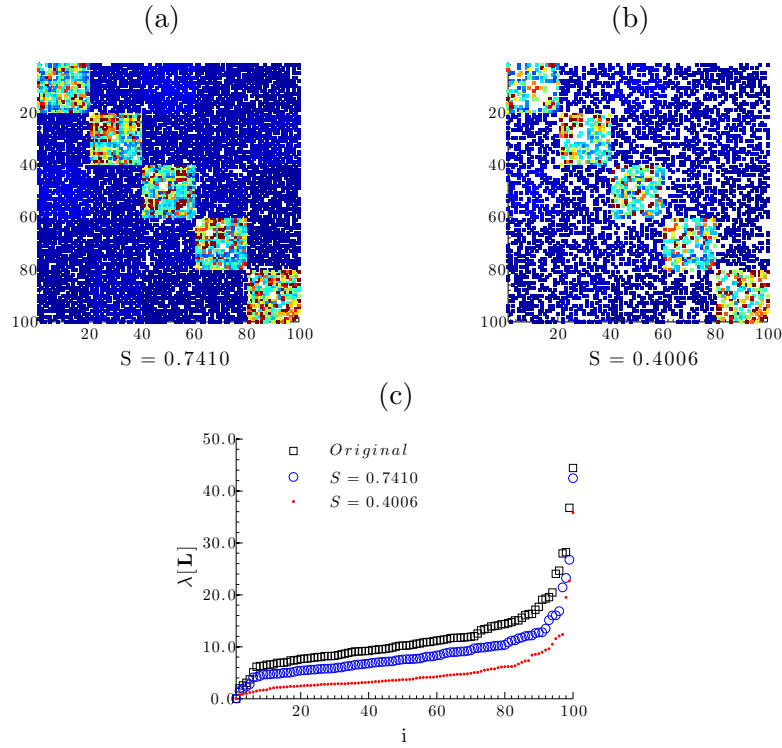


**Figure 11:** Sparsity patterns of the adjacency matrix for  $N = 100$  vortices with random cuts with sparsity (a)  $S = 0.7410$  and (b)  $S = 0.4006$ . The color in the sparsity patterns of the adjacency matrix indicates the adjacency weights  $\tilde{w}_{ij}$  for  $S = 0.7410$  and  $0.4006$ . (c) Eigenvalue spectra of Laplacian matrices of the randomly sparsified graphs with  $S = 0.7410$  and  $0.4006$  in comparison to the original graph. The legend for the sparsity patterns is similar to that of sparsity patterns in figure 3.

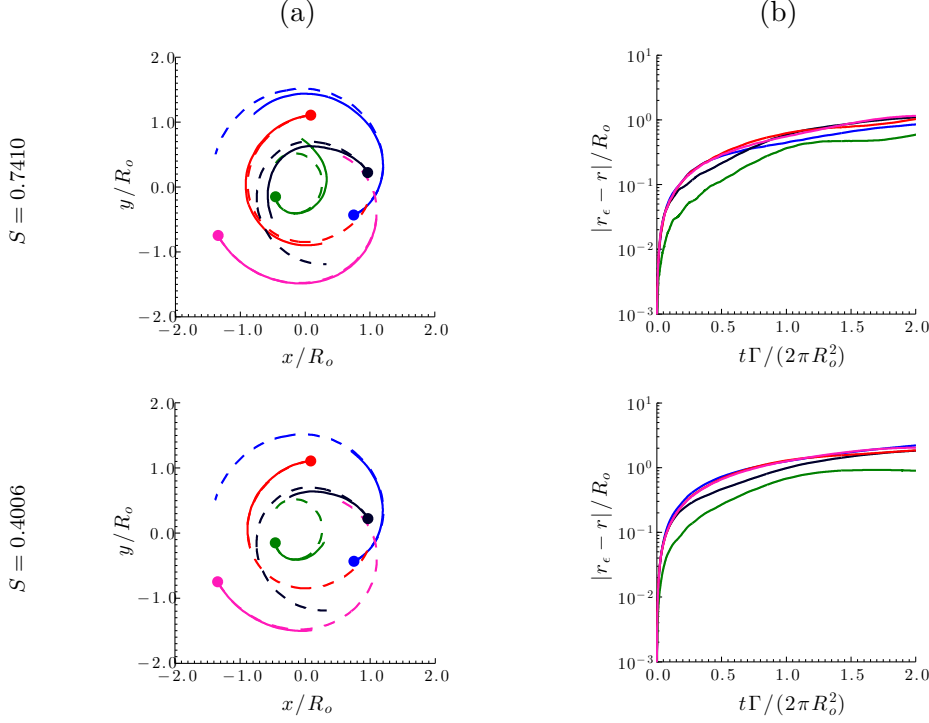


**Figure 12:** (a) Trajectories of the centroids and (b) error in position of centroids (right) of the vortex clusters based on random cuts with sparsity  $S = 0.7410$  and  $0.4006$  for  $N = 100$ ,  $\bar{\kappa} = 0.1$ .

as expected. This is due to the loss of induced velocity with the absence of weight redistribution from random sparsification. Spectral sparsification, on the other hand, redistributes the weights to prevent the loss of the overall interactions amongst the set of point vortices.

It is well known that fast multipole methods [31] can also reduce the  $\mathcal{O}(N^2)$  velocity evaluation significantly. The particle-box and box-box schemes reduce the computational complexity from  $\mathcal{O}(N^2)$  to  $\mathcal{O}(N \log(N))$  and  $\mathcal{O}(N)$ , respectively. As seen in this section, spectral sparsification reduces the computational load to  $\mathcal{O}(N \log(N))$  for computing the velocity of the vortices. Fast multipole methods approximate the effect of cluster of particles at a certain distance by multipole expansions and organizing the particles to a hierarchy of clusters [32]. In order to compensate for the sparsified connections in spectral sparsification, the weights are redistributed among the other edge connections to compute the sparsified dynamics. In an analogy to fast multipole methods, the interaction list depends on the connections that have direct impact on the vortices and computational accuracy may degrade when the vortices move in space. Similar to reconstruction of tree data structures in fast multipole methods, performing resparsification periodically increases the accuracy by re-evaluating the associated weights as the positions of the vortices evolve over time. We note that even with sparsification, invariants of discrete vortices are conserved as discussed below.

## 2.5 Conservation Properties

For a discrete set of point vortices, angular impulse and linear impulse are among the conserved quantities. The coordinates of center of vorticity obtained from linear impulse and the length of dispersion about the center of vorticity obtained from angular impulse, when the strength of vortices is of the same sign, remain constant. The center of vorticity  $(X, Y)$  and length of dispersion of

vorticity  $D$  are given by

$$X = \frac{\sum_{i=1}^N \kappa_i x_i}{\sum_{j=1}^N \kappa_j}, \quad Y = \frac{\sum_{i=1}^N \kappa_i y_i}{\sum_{j=1}^N \kappa_j}, \quad (13)$$

$$D^2 = \frac{\sum_{i=1}^N \kappa_i \{(x_i - X)^2 + (y_i - Y)^2\}}{\sum_{j=1}^N \kappa_j}, \quad (14)$$

where  $\kappa_i$  is the strength of the  $i$ -th vortex and  $(x, y)$  are the vortex positions [33, 19]. The circulation for  $n$  vortices in a cluster is  $\Gamma = n\bar{\kappa}$ . The total circulation of the system of  $n_c = 5$  clusters is given by  $\Gamma_t = \sum_{i=1}^N \kappa_i = n_c \Gamma$ . Another conserved quantity is the Hamiltonian. The Hamiltonian is defined as the interaction energy of the system of point vortices and is given by

$$H = -\frac{1}{4\pi} \sum_{i,j=1, i \neq j}^N \kappa_i \kappa_j \log \sqrt{(x_i - x_j)^2 + (y_i - y_j)^2}. \quad (15)$$

We non-dimensionalize the Hamiltonian using the total circulation of  $n_c$  clusters and the average radial distance of centroid of the clusters at initial time  $R_o$ .

We compare the error in the Hamiltonian  $(H_\epsilon(r/R_o) - H(r/R_o))/\Gamma_t^2$ , the center of vorticity  $((X_\epsilon - X)/R_o, (Y_\epsilon - Y)/R_o)$ , and the square of length of dispersion of vorticity  $(D_\epsilon^2 - D^2)/R_o^2$  for approximation orders of  $\epsilon = 0.5$  and 1 over time in figure 13. The preservation of center of vorticity and length of dispersion implies the conservation of linear and angular impulse. Here, the variables with subscript  $\epsilon$  denote those based on a sparsified model. We observe that the error in the Hamiltonian is of  $\mathcal{O}(10^{-4})$  for  $\epsilon = 0.5$  and  $\mathcal{O}(10^{-3})$  for  $\epsilon = 1$ . The error in the square of dispersion is of  $\mathcal{O}(10^{-6})$  while the error in the center of vorticity is of  $\mathcal{O}(10^{-8})$  with sparsification. While not shown, resparsification of these vortices periodically performed at every  $(0.1t\Gamma/2\pi R_o^2)$  and  $(0.01t\Gamma/2\pi R_o^2)$  maintain similar error levels for the invariants. We also note that the circulation of each vortices has not been altered, which conserves the individual and overall circulation over time.

As seen in §2.2, sparsification by effective resistance is based on the energy-minimization principle. The effective resistance is defined such that the total energy of the system remains constant. This is reflected well in the conservation of the Hamiltonian representing the interaction energy of the discrete point vortices. In addition, sparsification preserves other invariants including linear and angular impulse of the discrete set of point vortices. We note in passing that even with resparsification, the invariants were observed to be conserved. The conservation of the invariants for the sparse configurations further encourages the applicability of sparsification strategies on discrete vortex dynamics.

## 2.6 Sparsified-Dynamics Model and Reduced-Order Model

We comment on the similarities and differences between the present sparsified-dynamics model and the reduced-order model. Both models share the general objective of deriving a model that captures the full-order physics in a distilled manner. Reduced-order models achieve such goals by reducing the dimension of the state variable. One such technique is the Galerkin projection of the Navier–Stokes equations using a set of spatial bases [34, 35], such as those determined from POD [36, 37]. One can further consider incorporating the effect of input and output dynamics by using balanced truncation or the eigensystem realization algorithm [38, 39]. The resulting reduced-order models are generally described by ordinary-differential equations for the temporal coefficients with reduced dimensions.

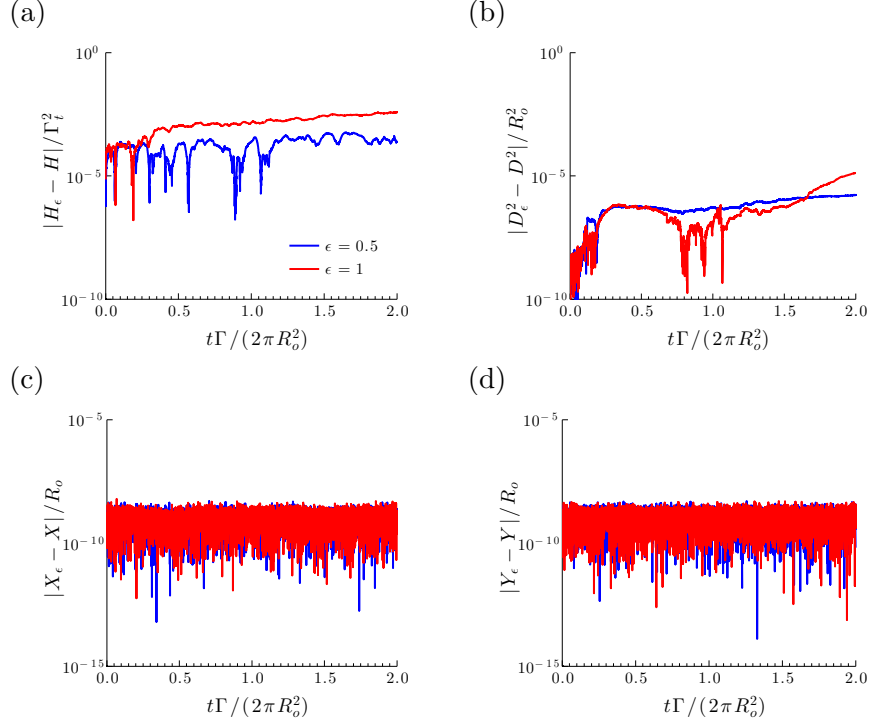


**Figure 13:** Error in the (a) Hamiltonian, (b) square of length of dispersion, (c)  $x$ -position of center of vorticity and (d)  $y$ -position of center of vorticity based on single sparsification for  $N = 100$ ,  $\bar{\kappa} = 0.1$  and  $\epsilon = \{0.5, 1\}$ .

On the other hand, the present sparsified-dynamics model does not reduce the dimensionality of the state variable. We instead focus on reducing the number of connections used to capture the overall dynamics of the fluid flow. The reduction in the number of connections is performed based on the concepts from network analysis and graph theory. Although we cut a large number of the edges in the graph representation of the dynamical interaction, we redistribute the weights associated with the edges to maintain properties of the graph. This procedure is based upon approximating the spectral properties of the graph and does not require selecting the spatial basis functions unlike the Galerkin-projection based models. One nice feature of the sparsified-dynamics model is its ability to conserve physical variables such as the Hamiltonian, angular impulse, and linear impulse, as discussed previously. Hence, the sparsified dynamics is able to predict the full dynamics as demonstrated by the example with discrete vortices. By highlighting the interactions amongst a set of vortices, we are able to determine which interactions amongst the vortices are important in guiding the overall motion of vortices.

We believe the sparsified-dynamics model has promising potential to model various types of fluid flow by considering the modal structures as a abstraction of graph nodes. The application of sparsified dynamics models towards flow control problems may also become fruitful as the computational time necessary to capture the complex behavior of the flow is reduced and the interaction of nodes or flow structures are well-captured, which has been a lacking feature in linear dynamics model and linear stability analysis. We anticipate that the presently proposed model can lead to potential feedback control of fluid flow [40, 41] but with nonlinear interactions emphasized. One of the open questions in extending the sparsified dynamics model for a wide variety of fluid flow problems is the choice of the variables or modes to be used for graph nodes. This issue is currently being examined and will be reported in upcoming studies.



### 3 Energy Transfer in Modal Network of Fluid Flow

In the above discrete vortex dynamics problem, we examined the collective behavior of a set of potential vortices using network analysis. Next, let us study the continuous representation of fluid flow using modal analysis with Galerkin projection. In this section, we consider the example of two-dimensional incompressible flow over a cylinder at a diameter-based Reynolds number of  $Re = 100$ . We construct an empirical Galerkin model based on POD (Karhunen–Loeve) expansion [42] of the snapshots of data gathered from direct numerical simulation of incompressible flow over a cylinder using the immersed boundary projection method [43, 44] as shown in figure 14. The work presented below is founded on the Galerkin-based model of Noack et al. [45, 46, 47].

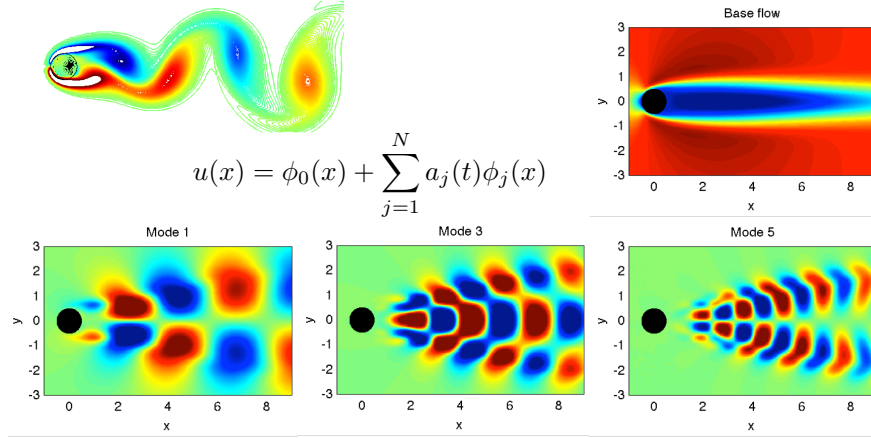


Figure 14: Unsteady cylinder flow at  $Re = 100$  and its POD modes.

#### 3.1 Modal Energy Interaction Analysis

To characterize a continuous representation of the flow field on a network, we take the finite Galerkin approximation of velocity field

$$\mathbf{u}(\mathbf{x}, t) \approx \mathbf{u}^{(N)} = \mathbf{u}_0(\mathbf{x}) + \sum_{i=1}^N a_i(t) \phi_i(\mathbf{x}) \quad (16)$$

where  $\mathbf{u}_0$  is the mean velocity field,  $\phi_i$  are the POD modes, and

$$a_i = (\mathbf{u} - \mathbf{u}_0, \phi_i) \quad (17)$$

are the generalized Fourier coefficients. Here,  $(a, b)$  denotes the inner product on the computational domain. Mode pairs with alternating symmetry properties can be computed from proper orthogonal decomposition (POD) and the energy of the modes are given by

$$\lambda_i = \langle (\mathbf{u} - \mathbf{u}_0, \phi_i)^2 \rangle = \langle a_i^2 \rangle, \quad (18)$$

where  $\langle \cdot \rangle$  represents time average. The kinetic energy of the  $i$ th mode is given by  $K_i = \lambda_i/2$  and the variation in the kinetic energy is given by  $K = \frac{1}{2} \langle (\mathbf{u}', \mathbf{u}') \rangle$  computed from the velocity fluctuations  $\mathbf{u}' = \mathbf{u} - \mathbf{u}_0$ .

The Galerkin projection of the incompressible Navier-Stokes equations<sup>1</sup>

$$\frac{\partial \mathbf{u}}{\partial t} + \nabla \cdot (\mathbf{u} \mathbf{u}) = -\nabla p + \frac{1}{Re} \nabla^2 \mathbf{u} \quad (19)$$

<sup>1</sup>incompressibility is implicitly satisfied by the POD modes already.

onto the POD modes result in a reduced-order model equation given by

$$\dot{a}_i = P_i + \sum_{j=1}^N L_{ij} a_j + \sum_{j,k=1}^N C_{ijk} a_j a_k, \quad i = 1, 2, \dots, N, \quad (20)$$

where

$$\begin{aligned} P_i &= \frac{1}{Re} (\phi_i, \nabla^2 \mathbf{u}_0) - (\phi_i, \nabla \cdot (\mathbf{u}_0 \mathbf{u}_0)) \\ L_{ij} &= \frac{1}{Re} (\phi_i, \nabla^2 \phi_j) - (\phi_i, \nabla \cdot (\mathbf{u}_0 \phi_j)) - (\phi_i, \nabla \cdot (\phi_j \mathbf{u}_0)) \\ C_{ijk} &= -(\phi_i, \nabla \cdot (\phi_j \phi_k)). \end{aligned} \quad (21)$$

Here,  $P_i$ ,  $L_{ij}$  and  $C_{ijk}$  are the constant mean shift coefficient, linear Galerkin coefficient term, and quadratic Galerkin coefficient term, respectively.

As we are interested in the interactions between these modes, we track the energy pathways between modes within the flow. We use the finite time thermodynamics (FTT) formulation [46, 47] to deduce constitutive equations for energy and average modal amplitude. Using Reynolds decomposition, we can split the modal amplitude as  $a_i = \langle a_i \rangle + a'_i$ , where  $m_i = \langle a_i \rangle$  and  $E_i = \frac{1}{2} \langle (a'_i)^2 \rangle$ . The constitute equations are given by

$$\begin{aligned} 0 &= P_i + \sum_{j=1}^N L_{ij} m_j + \sum_{j,k=1}^N C_{ijk} m_j m_k + \sum_{j=1}^N 2C_{ijj} E_j \\ \dot{E}_i &= Q_i + T_i \end{aligned} \quad (22)$$

There are primarily two energy interactions taking place between the modes. One is external energy  $Q_i$  (interaction with the mean flow) and the other is internal energy  $T_i$  (transfer) between the modes. External energy is the primary source of energy in the flow derived from the mean flow. External energy is given by

$$\begin{aligned} Q_i &= 2 \left[ L_{ii} + \sum_{j=1}^N (C_{iij} + C_{iji}) m_j \right] E_i \\ &= 2 \left[ \frac{1}{Re} (\phi_i, \nabla^2 \phi_i) - (\phi_i, \nabla \cdot (\mathbf{u}_0 \phi_i)) - (\phi_i, \nabla \cdot (\phi_i \mathbf{u}_0)) + \sum_{j=1}^N (C_{iij} + C_{iji}) m_j \right] E_i. \end{aligned} \quad (23)$$

The external energy interactions consist of energy diffusion (first term), convection (second term) and production (third term).

The internal triadic interaction terms (Fick's law) are given by

$$T_{ijk} = \alpha \xi_{ijk} \sqrt{K_i K_j K_k} \left( 1 - \frac{3K_i}{K_i + K_j + K_k} \right), \quad (24)$$

where  $\xi_{ijk} = \frac{1}{6} (|C_{ijk}| + |C_{ikj}| + |C_{jik}| + |C_{jki}| + |C_{kji}| + |C_{kij}|)$  with  $C_{ijk} = -(\phi_i, \nabla \cdot (\phi_j \phi_k) + \phi_i, \nabla p_{jk})$  and the parameter  $\alpha$  is required for balancing the overall kinetic energy. Here, pressure fluctuations are decomposed as  $P = \sum_{j,k=1}^N p_{jk} a_j a_k$ . The internal triadic interaction energy can be computed as  $T_i = \sum_{j,k=1}^N T_{ijk}$ . The triadic interaction terms are energy conserving, i.e.,  $\sum_{i=1}^N T_i = 0$ .

### 3.2 Network Representation of Modal Energy Interaction

We can create network representation of the modal energy interaction discussed above. The vertices or nodes of the graph represent POD modes. The edges between the nodes indicate the transfer of energy between the modes with the weights denoting the magnitude of energy flow. Also, the orientation of the edges denotes the direction of flow of energy.

As geometric symmetry conditions lead to equipartition of energy, we combine pairwise modes in the flow, i.e.,  $\{(\phi_1, \phi_2), (\phi_3, \phi_4), \dots\}$ . Thus, external and internal energy interaction for mode pairs 1 and 2 are given by  $Q_{[1,2]} = Q_1 + Q_2$  and  $T_{[1,2]} = T_1 + T_2$ , respectively. Also, as the triadic interaction terms are energy conserving, we can reduce the number of edges on the graph. Based on the sign of the internal energy transfer term, we can classify the mode pairs into donors and recipients. As donor mode pairs transfer energy to the recipient mode pairs, negative sign of the transfer term indicates donors. Thus the network representation consists of mean flow, donor nodes and recipient nodes.

Based on these observations, we can construct the adjacency matrix for the modal graph representing energy flow  $\mathcal{G}_e$  with,

$$[\mathcal{A}_{\mathcal{G}_e}]_{ij} = \begin{cases} Q_{[j_1, j_2]} & \text{if } i = 0 \text{ and } j_1 > i, j_2 > i \\ -T_{[j_1, j_2]} & \text{if } i = 1 \text{ and } j_1 > i, j_2 > i \\ 0 & \text{otherwise} \end{cases} \quad (25)$$

where,  $j_1$  and  $j_2$  are mode pairs. In the above notation, index 0 indicates the mean flow and 1 indicates donor node.

### 3.3 Application to Linear to Nonlinear Transitional Flow

In this section, we apply the above discussion to study the growth of perturbation energy in base state for cylinder flow. We study the transition of fluid flow from the base state to nonlinear limit cycle. As the problem considered (incompressible flow at  $Re = 100$ ) is unstable, we compute the unstable steady state (base state) using the selective frequency damping technique [48].

Starting from the unstable steady state, we collect snapshots of the velocity field at every  $\Delta t = 0.1525$  during which time small numerical perturbations are monitored to grow. This interval is chosen based on spectral analysis (not shown) performed in the nonlinear regime to collect a minimum of 40 snapshots per period. Small fluctuations of the coefficient of lift  $C_L$  is observed near the unstable steady state. As time increases, these fluctuations increase and they saturate in the nonlinear regime. The growth of these fluctuations from the unstable steady state to the nonlinear (limit cycle) regime is shown in figure 15(a). We collect snapshots over  $N_p = 16$  periods. Based on previous literature [49], we choose number of modes  $N = 8$  for our study. The corresponding variations in the kinetic energy of the modes over time are given in figure 15(b).

Network representations of energy interactions between the modes at  $t = 30$  (linear), 60 (transitional), 90 (nonlinear limit cycle) are shown in figure 16. Directionality of energy transfer is indicated by arrows in the graph. We can clearly see that mode pairs 1 and 2 form the donor modes of the graph. As the windowed over which POD modes are extracts shifts over time in the present analysis, the POD modes changes along with the mean flow for the shown three flow regimes. The legend indicates the magnitude of the interactions in log scale. Also, we can observe that with increase in time, the magnitude of interaction with the mean increases, particularly, the energy transferred from the mean to the donor modes. Also, as the flow approaches the limit cycle, the contributions from and to the mean flow are nearly equal. The weights of the interactions are shown adjacent to the edges of the graph.

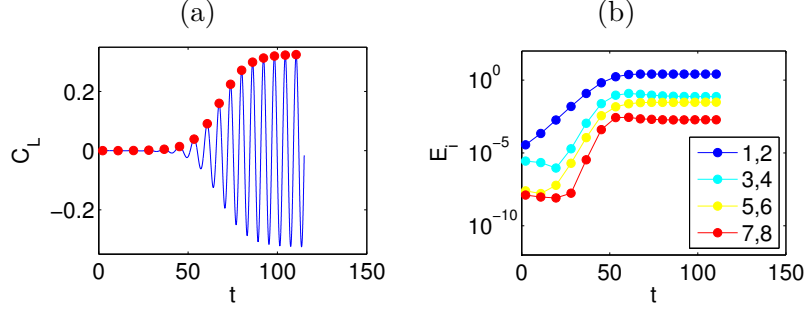


**Figure 15:** Variation of (a) coefficient of lift and (b) modal kinetic energy.

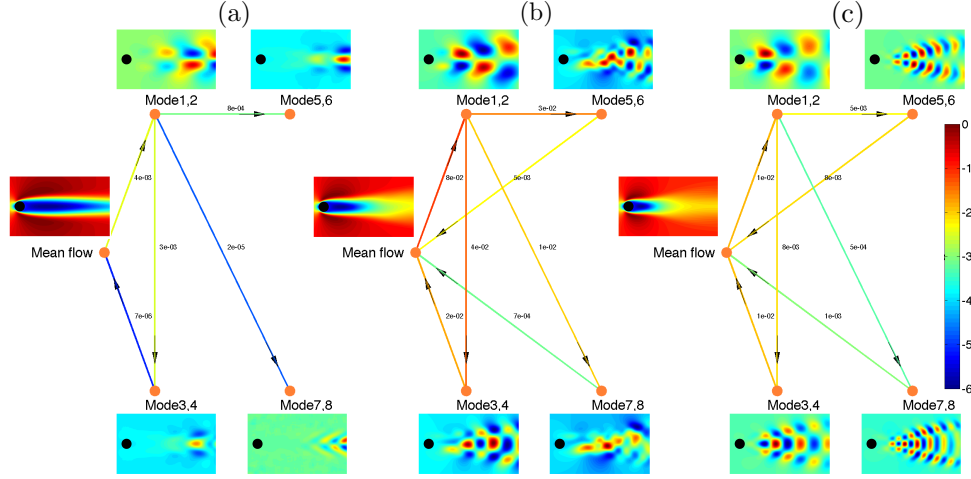


**Figure 16:** Network representation of modal energy interaction for cylinder flow transition to nonlinear regime using a windowed approach at (a)  $t = 30$ , (b)  $t = 60$  and (c)  $t = 90$ .

Using the windowed approach mentioned above, the POD modes and hence the nodes of the graph change in time. Also, the fixed point for the above analysis is the mean flow as opposed to the steady (base) state. This makes the analysis and hence network representation increasingly complex. For transient flow, Noack et al. [50] introduced the normalized mean field correction called the shift mode. This represents the shift of short-term time averaged flow away from the Karhunen-Loève space. The shift mode is constructed as follows.

$$\begin{aligned}\phi_{\Delta}^b &= (\mathbf{u}_0 - \mathbf{u}_s) - \sum_{i=1}^N (\mathbf{u}_0 - \mathbf{u}_s, \phi_i) \phi_i \\ \phi_{\Delta} &= \phi_{\Delta}^b / \|\phi_{\Delta}^b\|,\end{aligned}\tag{26}$$

where  $\phi_{\Delta}$  is the shift mode and  $\mathbf{u}_s$  is the base state (unstable steady state for cylinder flow at  $Re = 100$ ). Here, as the number of modes are 8, we consider the shift mode as the 9th mode in the governing (dynamical) equation.

We construct the nonlinear Galerkin model including the shift mode and integrate it in time. We show the phase portrait of variation in the shift mode with increasing time in figure 17(a). The variation in energy of the mode pairs is shown in figure 17(b) along with total energy variation in figure 17(c). We can see that the variation in modal energy in cylinder flow transition with the Galerkin model follows a similar trend to the windowed approach but the transition is delayed.

These results agree well with those obtained by Noack et al. [50]. As the transition is delayed compared to the windowed approach, we present the network representation of energy interactions between the modes at corresponding times as figure 16 for the Galerkin model, i.e.,  $t = 90, 195, 270$ . A shift mode is added to the graph as an additional node. The POD modes, mean and shift mode and hence the nodes of the energy graphs do not change with time. The modal interactions are similar to the windowed approach. We can observe an additional interaction from the shift mode to the mean flow especially in cylinder transition. This interaction however reduces as the flow reaches limit cycle behavior. As the POD modes change in the windowed approach, evolution of nodes of the graph becomes an additional concern. The Galerkin model approach reduces the complexity of problem by fixing the nodes of the graph. Addition of the shift mode as a node causes the fixed point of the model to be the correct base state as opposed to the mean flow for the windowed approach.

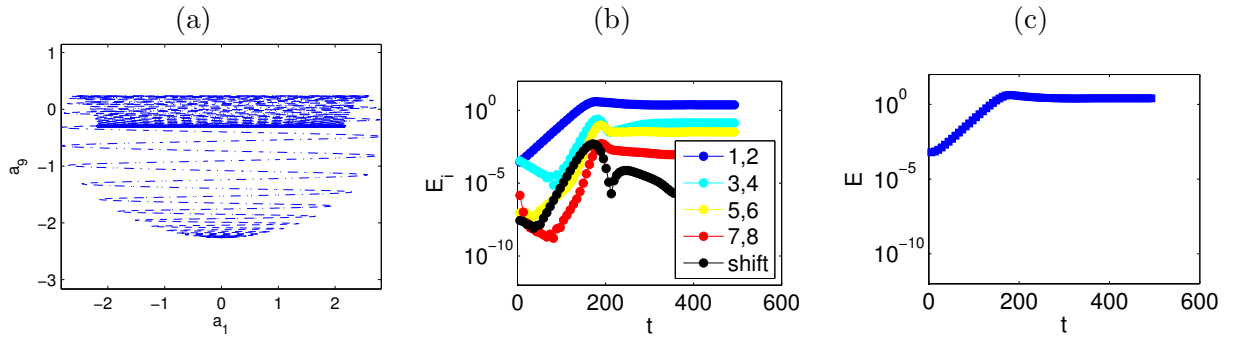


**Figure 17:** (a) Phase portrait of shift mode in cylinder flow transition. Variation in (b) modal kinetic energy and (c) total kinetic energy for galerkin model with shift mode.

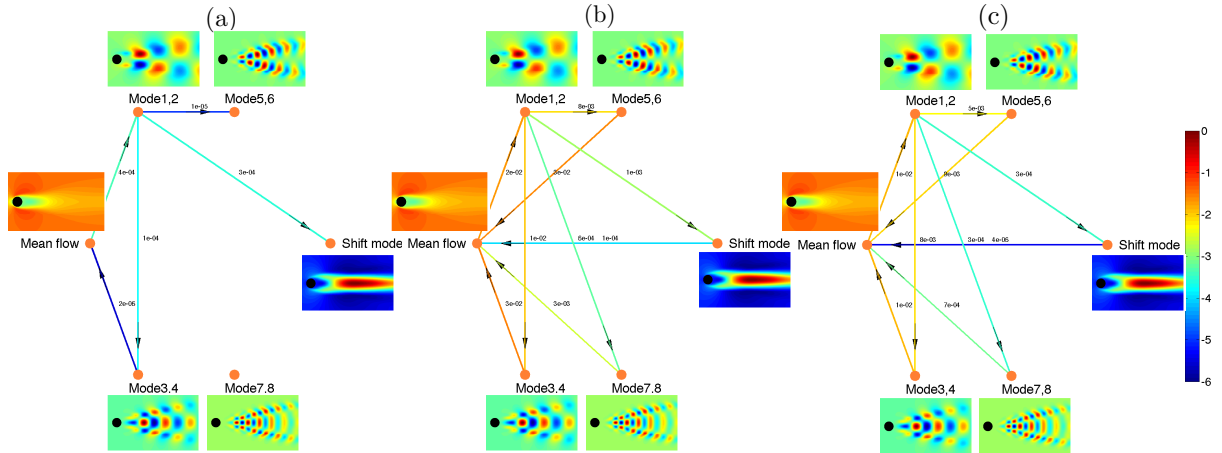


**Figure 18:** Network representation of modal energy interaction for cylinder flow transition to nonlinear regime using a shift mode at (a)  $t = 90$ , (b)  $t = 195$  and (c)  $t = 270$ .

### 3.4 Feedback Control of Modal Fluid Flow Network

We implement feedback control on the nonlinear Galerkin model and examine its implications on the modal energy interactions. First, let us observe the variation of the Galerkin coefficients for mode 1, 3 and shift mode 9 with no control added in figure 19(a). We add proportional control to

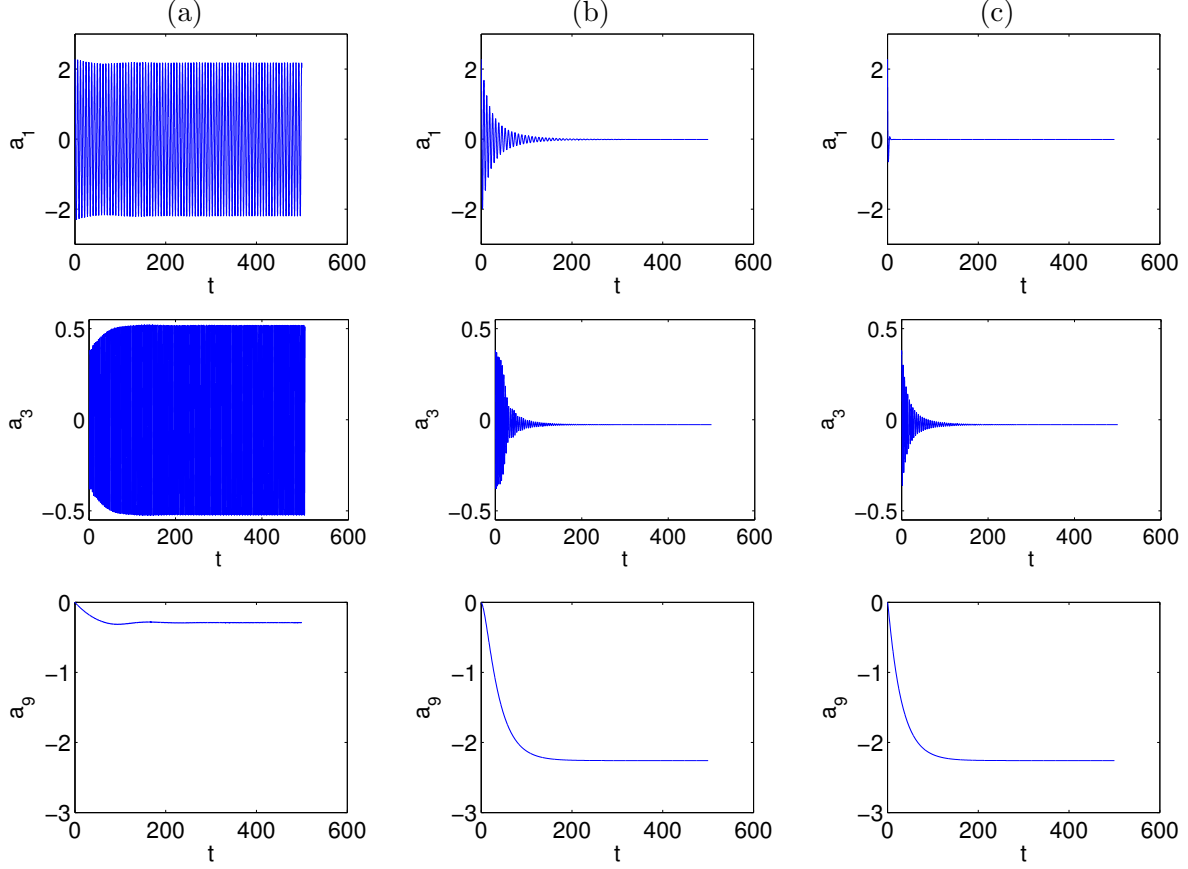


**Figure 19:** Variation of galerkin time coefficients of mode 1( $a_1$ ), mode 3( $a_3$ ), and shift mode 9( $a_9$ ) with (a) no control, (b) proportional control added to mode 1 and (c) optimal control (LQR) pinning mode 1.

POD mode 1 using proportional control based on Ziegler–Nichols tuning [51] and show the time history of temporal coefficients in figure 19(b). Proportional control with forcing solely on mode 1 guides the flow to base state, i.e., modal time coefficients reduce to zero while the shift mode settles to a value obtained at base state. We also perform LQR (linear quadratic regulator) control on mode 1. For the LQR design, we consider the linearized governing equation as the state-space equation given by  $\dot{a}_i = \sum_{j=1}^N L_{ij}a_j + Bq$ , where  $q$  is the input. As forcing is introduced to mode 1,  $B_{11} = 1$  and all other entries of  $B$  are zero. Considering identity matrices for the LQR weights, we can compute the feedback term  $q = -L_{ij}^*a_j$ . The entries of the row 1 of  $L^*$  are non-zero as control is added to mode 1. We update the linear term in the governing equation as  $L - L^*$  for performing LQR control on the nonlinear governing equation, the results of which are shown in figure 19(c). We can see that optimal control (LQR) works very effectively and forces the flow to base state.

Proportional control added to mode 1 amounts to adding a force term to the Galerkin integrated equation for mode 1 as shown in figure 20(a). Network representation of energy interactions between the modes at three different times  $t = 65, 140, 220$  during transition from oscillatory (shedding) behavior to base state are shown in figure 20(b), (c) and (d). We can see that the magnitude of mean interaction decreases as time proceeds. The force term added to the node of the graph modifies its node weight and hence the overall energy interaction. Optimal control (LQR), on the other hand, amounts to subtracting an additional linear term from the Galerkin integrated equation. Network representation of energy interactions between the modes immediately obtained

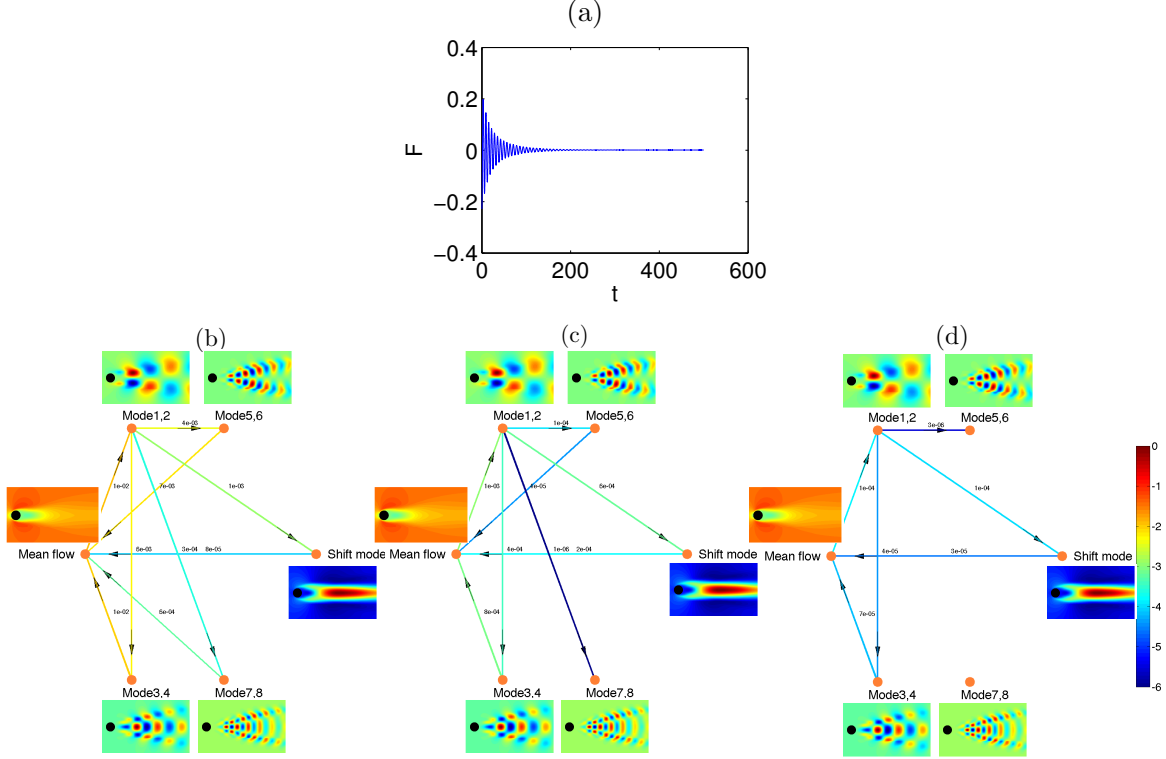


**Figure 20:** (a) Force term added to mode 1 (proportional control). Network representation of modal energy interaction with proportional control added to mode 1 at (b)  $t = 65$ , (c)  $t = 140$  and (d)  $t = 220$ .

after application of LQR control is shown in figure 21. We can see that the magnitude of mean interaction decreases.

In this study, we created (continuous) network representation of fluid flow based on the Galerkin-based model of Noack et al. [45, 46, 47]. The network representations aided in understanding of energy transfer between the modes in the flow. Thus, modal analysis allows us to capture energy transfer from one regime of flow to another. Transition of flow over a cylinder from base state to limit cycle behavior was examined to understand network flows and fundamental physics involved. In addition, control strategies were implemented to modify these energy interactions and force the flow to base state. We further plan to use graph-theoretic tools to extract information from network representations and modify the governing dynamics. In addition, we plan to extend the present analyses to high-dimensional fluid flow problems.

## 4 Two-Dimensional Turbulence Network

The above two network-model formulations have focused on discrete vortex dynamics and unsteady laminar flows. Here, we also apply network-based analysis to turbulent flows. In particular, we extend the Biot–Savart based formulation discussed in Section 2 to two-dimensional homogeneous isotropic turbulence [52, 53]. Here, we analyze two-dimensional turbulence by extracting the underlying network structure that captures the dominant vortex interactions. Furthermore, we show that two-dimensional turbulence has a scale-free network structure similar to other networks seen in nature [54].

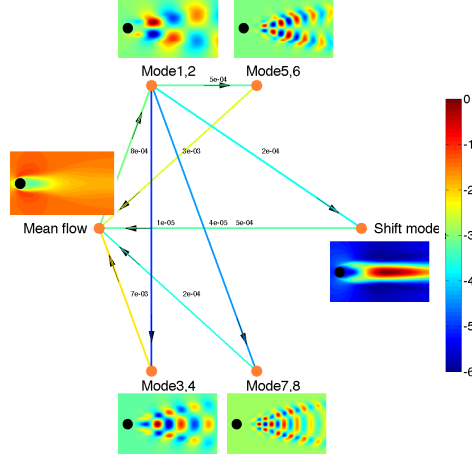


**Figure 21:** Network representation of modal energy interaction for optimal control (LQR) after one period of oscillation.

#### 4.1 Network Analysis Setup

Network-based modeling of vortex interactions presented in Section 2 was able to extract the dominant vortical network for a group of discrete vortices [55]. This was performed by constructing a model based on the Biot–Savart law by observing that a vortex influences the motion of all other vortices except for itself. The sum of the induced velocities determines how each individual vortex advects in the flow field. The strength of the interaction between two vortices in the flow field is quantified by the induced velocity  $u_\theta$ . The induced velocity from vortex  $i$  on vortex  $j$  is  $u_{\theta,i \rightarrow j} = \gamma_i / (2\pi r_{ij})$ , where the circulation of the  $i$ -th vortex is  $\gamma_i$  and the distance between vortices  $i$  and  $j$  is  $r_{ij} = |x_i - x_j|$ . Based on the induced velocity between two vortices, the adjacency matrix can be defined as  $A_{ij} = \frac{1}{2}(|\gamma_i| + |\gamma_j|)/r_{ij}$ . This measure of interaction is defined to be arithmetic average of the induced velocity (without the factor of  $2\pi$ ). The geometric average  $A_{ij} = \sqrt{|\gamma_i \gamma_j|}/r_{ij}$  has also been considered providing similar results. The key network structure was determined by performing graph sparsification on the full vortex interaction network using the above adjacency definition [55].

In the present study, we consider the use of network analysis to identify the underlying network

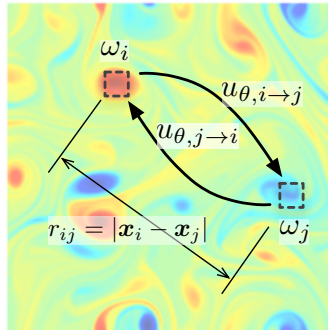


**Figure 22:** Interaction of fluid elements in two-dimensional turbulence. The vortical interaction between elements  $i$  and  $j$  having vorticity  $\omega_i$  and  $\omega_j$  can be quantified through the induced velocities  $u_{\theta,i \rightarrow j}$  and  $u_{\theta,j \rightarrow i}$ . The velocity induced by element  $i$  onto  $j$  is  $u_{\theta,i \rightarrow j} = \omega_i S / (2\pi r_{ij})$ , where  $S$  is the area of the fluid element ( $\gamma_i = \omega_i S$ ). The vorticity is shown in the background as a contour plot.



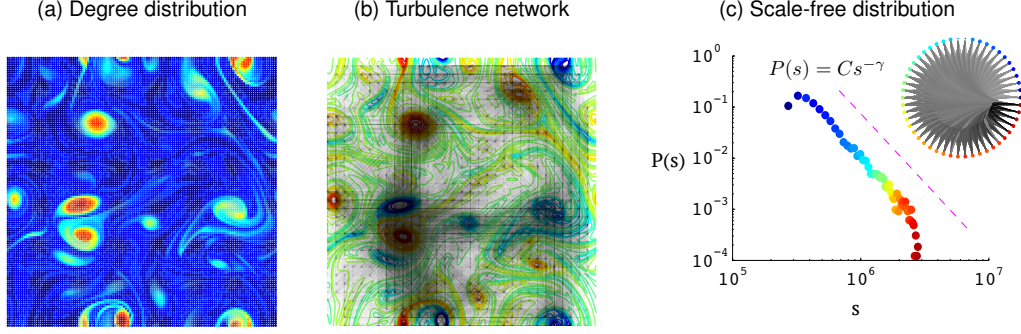


**Figure 23:** The connectivity distribution shown over the physical domain for two-dimensional turbulent flow (panel a). Vortex cores having a high degree of connectivity act as hubs in the turbulent vortical network. Depiction of scale-free network structure over the Eulerian node points is shown with the darkness of the network edges corresponding to the values of the adjacency elements (panel b). A majority of the key edges are seen within the vortical structures and amongst large-scale structures. The corresponding degree distribution plot exhibits scale-free characteristics with  $P \approx Ck^{-\gamma \pm \Delta\gamma}$  (panel c). The inset shows the circos plot of the turbulent network depicting rotational symmetry. Panels (a) and (c) share the same contour level.

structure and characteristics of two-dimensional unforced homogeneous isotropic turbulence. The adjacency matrix is constructed by evaluating the local vorticity (circulation) of fluid elements in an Eulerian discretization of a bi-periodic domain as illustrated in figure 22. Eulerian grid points are taken to be nodes on the network and edges are characterized by the vortical interactions between the nodes. The two-dimensional turbulent flow is simulated by numerically solving the vorticity transport equation using a Fourier pseudo-spectral method [56].

## 4.2 Scale-Free Characteristics of Two-Dimensional Turbulence

Based on the adjacency matrix, we can identify which fluid elements have high degree of connections (interactions). Vortices with higher strengths, corresponding to large circulation, are generally larger and they affect smaller vortices as illustrated in figure 23(a). Hence larger stronger vortices seen in red act as network hubs. Note that these strong vortices induce velocity over long distances. In contrast, fluid elements corresponding to smaller, weaker eddies, shown in blue, only have influence in their local vicinity. The vortical interaction network exhibits a vast network mostly connecting the vortical hubs with localized connections appearing for the weaker and smaller eddies figure 23(b). From preliminary analysis, the degree distribution of the two-dimensional isotropic turbulence network is found to be well represented by a power-law distribution  $P \sim k^{-\gamma}$  with  $\gamma = 3.0 \pm 0.25$  as shown in figure 23(c). This distribution exhibits scale-free characteristics for the turbulence network. It is interesting to observe that the scale-free nature of the two-dimensional turbulence also shares commonality with other scale-free networks observed in various fields of natural and social sciences. The current observation reveals that a scale-free network can describe two-dimensional turbulence comprised of vortices of varying scales and strengths. This behavior cascades down to smaller scales. Visualization of the degree distribution with a circos plot (panel c) clearly shows the universal scale-free features of the turbulence network, as evident from the near rotational symmetry.

Characterizing a turbulent flow as a scale-free network enables us to view turbulent interactions in an intuitive manner. Network science provides insight into how components of a large system are interconnected. It is well known from network analysis that scale-free networks are resilient to random perturbations. However, attacks concentrated at network hubs can affect network dynamics in a detrimental manner, as seen in the examples of aircraft flight and Internet network operations.

This provides us with intuitive explanation that turbulent flows will be resilient against small-scale forcing while the global behavior can be easily modified by large-scale forcing targeting large vortex cores. This refreshing viewpoint allows us to provide mathematical guidance into the possibility of taming turbulent flows, which will impact a wide spectrum of engineering and scientific fluid flow applications.

## 5 Summary

In this study, unsteady fluid flows were modeled to highlight the vortical and modal interactions using network-based approaches. Three canonical fluid flow problems were chosen to develop the network-based framework. First, we examined in detail the discrete vortex dynamics to capture the collective behavior of a large number of vortices. Graph sparsification was utilized to extract the important vortical interaction network and yielded the sparsified dynamics model. This model was found to accurately capture the global motion of vortices and with significant reduction in computational cost. Second, the modal-interaction network was developed based on the work by Noack et al. to examine how perturbations and control inputs propagate over the modal network. We anticipate that this type of approach will facilitate the analysis of higher-dimensional complex fluid flows. At last, network-based characterization of two-dimensional homogenous turbulence was performed. Preliminary analysis has revealed that two-dimensional turbulence possesses a scale-free structure. This finding reveals insights into the robustness of turbulence network and how we may possibly control or modify the dynamics of turbulence. The fundamental findings and development of network-based framework from this study should enable future work in analyzing, modeling, and controlling a variety of fluid flows by leveraging the knowledge of interactions within unsteady fluid flows.

## 6 Personnel

The following members were involved in this STIR research effort:

---

Faculty:	Kunihiko Taira
Postdoctoral Associate:	Alejandro Rivera-Alvarez
Graduate Student:	Aditya G. Nair
Collaborator (Section 4):	Steven Brunton (University of Washington)

---

## 7 Acknowledgments

This research was supported by the U.S. Army Research Office (Award Number W911NF-14-1-0386, Program Manager: Dr. Samuel Stanton). Part of the work was also supported by the U.S. Air Force Office of Scientific Research (Award Number FA9550-13-1-0183, Program Manager: Dr. Douglas Smith).

## References

- [1] Bollobás, B., *Modern graph theory*, Springer, 1998.
- [2] Newman, M. E. J., *Networks: an introduction*, Oxford Univ. Press, 2010.
- [3] Duarte-Cavajalino, J. M., Jahanshad, N., Lenglet, C., McMahon, K. L., de Zubicaray, G. I., Martin, N. G., Wright, M. J., Thompson, P. M., and Sapiro, G., “Hierarchical topological network analysis of anatomical human brain connectivity and differences related to sex and kinship,” *NeuroImage*, Vol. 59, 2012, pp. 3784–3804.

- [4] Owen, J. P., Li, Y.-O., Ziv, E., Strominger, Z., Gold, J., Bukhpun, P., Wakahiro, M., Friedman, E. J., Sherr, E. H., and Mukherjee, P., “The structural connectome of the human brain in agenesis of the corpus callosum,” *NeuroImage*, Vol. 70, 2013, pp. 340–355.
- [5] Morris, M., “Epidemiology and social networks - modeling structured diffusion,” *Sociol. Method Res.*, Vol. 22, 1993, pp. 99–126.
- [6] Lloyd-Smith, J., Schreiber, S., Kopp, P., and Getz, W., “Superspreading and the effect of individual variation on disease emergence,” *Nature*, Vol. 438, 2005, pp. 355–359.
- [7] Glass, R. J., Glass, L. M., Beyeler, W. E., and Min, H. J., “Targeted social distancing design for pandemic influenza,” *Emerg. Infect. Diseases*, Vol. 12, No. 11, 2006, pp. 1671–1681.
- [8] Cauchemez, S., A, B., Marchbanks, T. L., Fagan, R. P., S. Ostroff, N. M. F., Swerdlow, D., and working group, P. H., “Role of social networks in shaping disease transmission during a community outbreak of 2009 H1N1 pandemic influenza,” *Proceedings of the National Academy of Sciences*, Vol. 108, No. 7, 2011, pp. 2825–2830.
- [9] Salathé, M. and Jones, J. H., “Dynamics and control of diseases in networks with community structure,” *PLoS Comput. Bio.*, Vol. 6, No. 4, 2010, pp. e1000736.
- [10] Robinson, K., Cohen, T., and Colijn, C., “The dynamics of sexual contact networks: effects on disease spread and control,” *Theo. Popul. Bio.*, Vol. 81, 2012, pp. 89–96.
- [11] Porter, M. A., Mucha, P. J., Newman, M. E. J., and Warmbrand, C. M., “A network analysis of committees in the U.S. House of Representatives,” *Proc. Nat. Acad. Sci.*, Vol. 102, No. 20, 2005, pp. 7057–7062.
- [12] Chen, W. K., *The Electrical Engineering Handbook*, Elsevier Science, 2004.
- [13] Ferziger, J. H. and Perić, M., *Computational methods for fluid dynamics*, Springer, Berlin, 3rd ed., 2002.
- [14] Schmid, P. J. and Henningson, D. S., *Stability and transition in shear flows*, Springer, 2001.
- [15] Theofilis, V., “Global linear instability,” *Annu. Rev. Fluid Mech.*, Vol. 43, 2011, pp. 319–352.
- [16] Chung, F., *Spectral Graph Theory*, American Mathematical Society, 1997.
- [17] Mohar, B., “The Laplacian spectrum of graphs,” *Graph theory, combinatorics, and applications*, edited by Y. Alavi, G. Chartrand, O. Ollermann, and A. Schwenk, Wiley, New York, 1991, pp. 871–898.
- [18] Saffman, P. G., *Vortex dynamics*, Cambridge Univ. Press, 1992.
- [19] Newton, P. K., *The N-vortex problem: analytical techniques*, Vol. 145 of *Applied Mathematical Sciences*, Springer, 2001.
- [20] Spielman, D. A. and Teng, S.-H., “Spectral sparsification of graphs,” *SIAM J. Comput.*, Vol. 40, No. 4, 2011, pp. 981–1025.
- [21] Peleg, D. and Ullman, J., “An optimal synchronizer for the hypercube,” *SIAM Journal on computing*, Vol. 18, No. 4, 1989, pp. 740–747.

- [22] Benczúr, A. and Karger, D. R., “Approximating  $s - t$  Minimum Cuts in  $\mathcal{O}(n^2)$  time,” *Proceedings of the twenty-eighth annual ACM symposium on Theory of computing*, ACM, 1996, pp. 47–55.
- [23] Kelner, J. and Levin, A., “Spectral sparsification in the semi-streaming setting,” *Leibniz International Proceedings in Informatics (LIPIcs) series*, Vol. 9, 2011, pp. 440–451.
- [24] Spielman, D. A. and Srivastava, N., “Graph sparsification by effective resistances,” *SIAM J. Comput.*, Vol. 40, No. 6, 2011, pp. 1913–1926.
- [25] Srivastava, N., *Spectral sparsification and restricted invertibility*, Ph.D. thesis, Yale University, 2010.
- [26] Klein, D. J. and Randić, M., “Resistance distance,” *Journal of Mathematical Chemistry*, Vol. 12, No. 1, 1993, pp. 81–95.
- [27] Ellens, W., Spieksma, F., Van Mieghem, P., Jamakovic, A., and Kooij, R., “Effective graph resistance,” *Linear algebra and its applications*, Vol. 435, No. 10, 2011, pp. 2491–2506.
- [28] Mieghem, P. V., *Graph spectra for complex networks*, Cambridge University Press, 2011.
- [29] Newman, M. E. J., “Fast algorithm for detecting community structure in networks,” *Physical review E*, Vol. 69, 2004, pp. 066133.
- [30] Kaiser, E., Noack, B. R., Cordier, L., Spohn, A., Segond, M., Abel, M., Daviller, G., and Niven, R. K., “Cluster-based reduced-order modelling of a mixing layer,” *Journal of Fluid Mechanics*, Vol. 754, 2014, pp. 365–414.
- [31] Greengard, L. and Rokhlin, V., “A fast algorithm for particle summations,” *J. Comput. Phys.*, Vol. 73, 1987, pp. 325–348.
- [32] Cottet, G.-H. and Koumoutsakos, P. D., *Vortex methods: theory and practice*, Cambridge Univ. Press, 2000.
- [33] Batchelor, G., *An introduction to fluid dynamics*, Cambridge university press, 2000.
- [34] Noack, B. R., Papas, P., and Monkewitz, P. A., “The need for a pressure-term representation in empirical Galerkin models of incompressible shear flows,” *J. Fluid Mech.*, Vol. 523, 2005, pp. 339–365.
- [35] Rowley, C., Colonius, T., and Murray, R., “Model reduction for compressible flows using POD and Galerkin projection,” *Physica D: Nonlinear Phenomena*, Vol. 189, No. 1, 2004, pp. 115–129.
- [36] Berkooz, G., Holmes, P., and Lumley, J., “The proper orthogonal decomposition in the analysis of turbulent flows,” *Annual review of fluid mechanics*, Vol. 25, No. 1, 1993, pp. 539–575.
- [37] Holmes, P., Lumley, J. L., and Berkooz, G., *Turbulence, coherent structures, dynamical systems and symmetry*, Cambridge Univ. Press, 1996.
- [38] Rowley, C. W., “Model reduction for fluids, using balanced proper orthogonal decomposition,” *Int. J. Bif. Chaos*, Vol. 15, No. 3, 2005, pp. 997–1013.

- [39] Ma, Z., Ahuja, S., and Rowley, C. W., “Reduced order models for control of fluids using the Eigensystem Realization Algorithm,” *Theo. Comp. Fluid Dyn.*, Vol. 25, No. 1, 2009, pp. 233–247.
- [40] Bagheri, S., Hoepffner, J., Schmid, P., and Henningson, D., “Input-output analysis and control design applied to a linear model of spatially developing flows,” *Applied Mechanics Reviews*, Vol. 62, No. 2, 2009.
- [41] Ahuja, S. and Rowley, C. W., “Feedback control of unstable steady states of flow past a flat plate using reduced-order estimators,” *J. Fluid Mech.*, Vol. 645, 2010, pp. 447–478.
- [42] Sirovich, L., “Turbulence and the dynamics of coherent structures, Parts I-III,” *Q. Appl. Math.*, Vol. XLV, 1987, pp. 561–590.
- [43] Taira, K. and Colonius, T., “The immersed boundary method: a projection approach,” *J. Comput. Phys.*, Vol. 225, 2007, pp. 2118–2137.
- [44] Colonius, T. and Taira, K., “A fast immersed boundary method using a nullspace approach and multi-domain far-field boundary conditions,” *Comput. Methods Appl. Mech. Engrg.*, Vol. 197, 2008, pp. 2131–2146.
- [45] Noack, B. R., Afanasiev, K., Morzyński, M., Tadmor, G., and Thiele, F., “A hierarchy of low-dimensional models for the transient and post-transient cylinder wake,” *J. Fluid Mech.*, Vol. 497, 2003, pp. 335–363.
- [46] Noack, B. R., Schlegel, M., Ahlborn, B., Mutschke, G., Morzyński, M., and Comte, P., “A finite-time thermodynamics of unsteady fluid flows,” *Journal of Non-Equilibrium Thermodynamics*, Vol. 33, No. 2, 2008, pp. 103–148.
- [47] Noack, B. R., Schlegel, M., Morzyński, M., and Tadmor, G., “System reduction strategy for Galerkin models of fluid flows,” *International Journal for Numerical Methods in Fluids*, Vol. 63, No. 2, 2010, pp. 231–248.
- [48] Åkervik, E., Brandt, L., Henningson, D. S., Hoepffner, J., Marxen, O., and Schlatter, P., “Steady solutions of the Navier-Stokes equations by selective frequency damping,” *Phys. Fluids*, Vol. 18, 2006, pp. 068102.
- [49] Deane, A., Kevrekidis, I., Karniadakis, G. E., and Orszag, S., “Low-dimensional models for complex geometry flows: Application to grooved channels and circular cylinders,” *Physics of Fluids A: Fluid Dynamics (1989-1993)*, Vol. 3, No. 10, 1991, pp. 2337–2354.
- [50] Noack, B., Afanasiev, K., Morzynski, M., Tadmor, G., and Thiele, F., “A hierarchy of low-dimensional models for the transient and post-transient cylinder wake,” *Journal of Fluid Mechanics*, Vol. 497, 2003, pp. 335–363.
- [51] Ziegler, J. G. and Nichols, N. B., “Optimum settings for automatic controllers,” *trans. ASME*, Vol. 64, No. 11, 1942.
- [52] Kraichnan, R. H. and Montgomery, D., “Two-dimensional turbulence,” *Rep. Prog. Phys.*, Vol. 43, 1980, pp. 547–619.
- [53] Boffetta, G. and Ecke, R. E., “Two-dimensional turbulence,” *Annu. Rev. Fluid Mech.*, Vol. 44, 2012, pp. 427–451.

- [54] Barabási, A.-L. and Albert, R., “Emergence of scaling in random networks,” *Science*, Vol. 286, 1999, pp. 509–512.
- [55] Nair, A. G. and Taira, K., “Network-theoretic approach to sparsified discrete vortex dynamics,” *J. Fluid Mech.*, Vol. 768, 2015, pp. 549–571.
- [56] Canuto, C., Hussaini, M. Y., Quarteroni, A., and Zang, T. A., *Spectral methods in fluid dynamics*, Springer-Verlag, New York, 1988.